

Methane emissions from China: a high-resolution inversion of TROPOMI satellite observations

Zichong Chen^{1*}, Daniel J. Jacob¹, Hannah Nesser¹, Melissa P. Sulprizio¹, Alba Lorente², Daniel J. Varon¹, Xiao Lu³, Lu Shen⁴, Zhen Qu¹, Elise Penn¹, and Xueying Yu⁵

¹Department of Earth and Planetary Sciences, Harvard University, Cambridge, MA, USA

²SRON Netherlands Institute for Space Research, Leiden, the Netherlands

³School of Atmospheric Sciences, Sun Yat-sen University, Zhuhai, Guangdong, China

⁴Department of Atmospheric and Oceanic Sciences, School of Physics, Peking University, Beijing, China

⁵Department of Soil, Water, and Climate, University of Minnesota, Saint Paul, MN, USA

10 *Correspondence to:* Zichong Chen (zchen1@g.harvard.edu)

Abstract. We quantify methane emissions in China and the contributions from different sectors by inverse analysis of 2019 TROPOMI satellite observations of atmospheric methane. The inversion uses as prior estimate the national sector-resolved anthropogenic emission inventory reported by the Chinese government to the United Nations Framework Convention on Climate Change (UNFCCC) and thus serves as a direct evaluation of that inventory. Emissions are optimized with a Gaussian mixture model (GMM) at up to $0.25^\circ \times 0.3125^\circ$ resolution. The optimization is done analytically assuming lognormally distributed errors on prior emissions. Errors and information content on the optimal estimates are obtained directly from the analytical solution and also through a 36-member inversion ensemble. Our optimal estimate for total anthropogenic emissions in China is 65.0 (57.7 - 68.4) Tg a^{-1} , where parentheses indicate uncertainty range. Contributions from individual sectors include 16.6 (15.6 - 17.6) Tg a^{-1} for coal, 2.3 (1.8 - 2.5) for oil, 0.29 (0.23 - 0.32) for gas, 17.8 (15.1 - 21.0) for livestock, 9.3 (8.2 - 9.9) for waste, 11.9 (10.7 - 12.7) for rice paddies, and 6.7 (5.8 - 7.1) for other sources. Our estimate is 21% higher than the Chinese inventory reported to the UNFCCC (53.6 Tg a^{-1}), reflecting upward corrections to emissions from oil (+147%), gas (+61%), livestock (+37%), waste (+41%), and rice paddies (+34%), but downward correction for coal (-15%). It is also higher than previous inverse studies (43 - 62 Tg a^{-1}) that used the much sparser GOSAT satellite observations and were conducted at coarser resolution. We are in particular better able to separate coal and rice emissions. Our higher livestock emissions are attributed largely to northern China where GOSAT has little sensitivity. Our higher waste emissions reflect at least in part a rapid growth in wastewater treatment in China. Underestimate of oil emissions in the UNFCCC report appears to reflect unaccounted super-emitting facilities. Gas emissions in China are mostly from distribution, in part because of low emission factors from production and in part because 42% of the gas is imported. Our estimate of emissions per unit of domestic gas production indicates a low life-cycle loss rate of 1.7 (1.3 - 1.9) %, which would imply net climate benefits from the current coal-to-gas energy transition in China. However, this small loss rate is somewhat misleading considering China's high gas imports, including from Turkmenistan where emission per unit of gas production is very high.

40

1. Introduction

Methane (CH₄) is a potent greenhouse gas with an atmospheric lifetime of 9.1 ± 0.9 years (Prather *et al.*, 2012). Its atmospheric concentration has nearly tripled since pre-industrial times because of anthropogenic emissions. The resulting radiative forcing from methane on an emission basis (including effects on tropospheric ozone, stratospheric water vapor, and carbon dioxide (CO₂)) is 1.21 W m^{-2} since the pre-industrial era, compared to 2.16 W m^{-2} for CO₂ (Naik *et al.*, 2021). Reducing methane emissions is a recognized priority under the Paris Agreement. As of January 2022, 111 countries have signed the Global Methane Pledge to reduce their methane emissions by 30% below 2020 levels by 2030 (<https://www.globalmethanepledge.org>).

50 As one of the major agricultural and energy production countries, China is a major contributor to global anthropogenic methane emissions. China is estimated to have emitted 46-74 Tg a⁻¹ out of a global anthropogenic source of 349-393 Tg a⁻¹ for the 2008-2017 decade (Saunio *et al.*, 2020), making it the top country for anthropogenic emissions (Worden *et al.*, 2022). According to the latest national emission inventory for 2014 submitted by the Chinese government to the United Nations Framework Convention on Climate Change (UNFCCC, 2020), China emitted 53.6 Tg a⁻¹ including contributions from coal mining (38%), livestock (24%), rice paddies (16%), landfills (7%), wastewater management (5%), oil/gas systems (2%), and other sources (8%). Emission inventories reported to the UNFCCC are ‘bottom-up’ estimates derived from activity data and
60 emission factors (EFs) per unit of activity, supplemented in some cases with more source-specific information. There are large uncertainties in these bottom-up estimates (Saunio *et al.*, 2020; Gao *et al.*, 2021). Different bottom-up national inventories for China as reported by Lin *et al.* (2021) ranged from 44.4 to 57.5 Tg a⁻¹ in 2010, with larger relative differences for individual sectors. These uncertainties make it difficult to set targets for reducing methane emissions.

The recent ‘coal-to-gas’ transition policy in China (Qin *et al.*, 2018) has raised growing awareness of oil/gas methane emissions, which are presently small but could grow rapidly. Gas is projected to account for 15% of total energy supply in China by 2030 (Gan *et al.*, 2020). It is crucial to quantify China’s oil/gas and coal methane emissions in order to assess the climate benefits of switching from coal to gas (Alvarez *et al.*, 2012, 2018). Chinese oil/gas emissions in the most recent version of the widely used bottom-up EDGAR v6 inventory for 2018 (3.4 Tg a⁻¹;
70 Crippa *et al.*, 2021) are much higher than the government report to UNFCCC (1.1 Tg a⁻¹), while coal emissions in EDGAR v6 (20.4 Tg a⁻¹) are consistent with the government report (19.5 Tg a⁻¹). Previous versions of EDGAR overestimated coal emissions from China (Bergamaschi *et al.*, 2013; Turner *et al.*, 2015).

Satellite observations of atmospheric methane in the shortwave infrared (SWIR) offer important ‘top-down’ information for evaluating bottom-up inventories and reducing uncertainty (Jacob *et al.*, 2016). Exploiting this information involves inversion of the observations with an atmospheric transport model relating emissions to atmospheric concentrations, and using the bottom-up inventory as prior information (Brasseur and Jacob, 2017). A number of global and regional inversions relevant to China have been conducted with satellite observations from the
80 Scanning Imaging Absorption Spectrometer for Atmospheric Chartography (SCIAMACHY) for 2003–2012 (Bergamaschi *et al.*, 2013; Houweling *et al.*, 2014) and the Greenhouse Gases Observing Satellite (GOSAT) for 2009-present (Alexe *et al.*, 2015; Turner *et al.*, 2015; Pandey *et al.*, 2016; Miller *et al.*, 2019; Maasakkers *et al.*, 2019; Y. Zhang *et al.*, 2021; Qu *et al.*, 2021; Deng *et al.*, 2022). The TROPospheric Monitoring Instrument (TROPOMI) satellite instrument launched in October 2017 provides global daily data with $5.5 \text{ km} \times 7 \text{ km}$ ($7 \text{ km} \times 7 \text{ km}$ before August 2019) pixel resolution, considerably increasing coverage relative to previous satellite

instruments (Hu et al., 2018; Lorente et al., 2021). Recent studies have used TROPOMI data in inverse analyses of methane emissions for North America (Y. Zhang et al., 2020; Shen et al., 2021) and globally (Qu et al., 2021; van Peet et al., 2021).

90 Here we use TROPOMI observations for 2019 to quantify methane emissions from China at up to $0.25^\circ \times 0.3125^\circ$ ($\sim 25 \times 25 \text{ km}^2$) resolution and with attribution to different source sectors. Our inversion uses the Chinese national inventory reported to the UNFCCC as prior information so that our results are directly relevant for evaluating that inventory. We apply an analytical solution to the Bayesian inference of methane emissions (Jacob et al., 2016), which has the advantage of providing closed-form error statistics and hence information content as part of the solution, and also allows us to conduct an ensemble of sensitivity inversions at no additional computational effort.

2. Data and Methods

100 We conduct the inversion of TROPOMI data for the full year of 2019 over the East Asia domain of Fig. 1 (15° - 55° N, 70° - 140° E) at up to $0.25^\circ \times 0.3125^\circ$ resolution. In this section we describe the TROPOMI observations (Sect. 2.1), the prior emission estimates (Sect. 2.2), the GEOS-Chem chemical transport model used as forward model for the inversion (Sect. 2.3), the analytical inversion method (Sect. 2.4), the sectoral attribution of inversion results (Sect. 2.5), and the ensemble of sensitivity inversions (Sect. 2.6).

2.1 TROPOMI observations

110 TROPOMI is onboard the polar sun-synchronous Sentinel-5 Precursor satellite with a $\sim 13:30$ local overpass time. The instrument observes methane columns by solar backscatter in the $2.3 \mu\text{m}$ absorption band with near-uniform sensitivity down to the surface. The column-averaged dry-air methane mixing ratio (XCH_4) is retrieved with a full-physics algorithm (Butz et al., 2011) together with surface and atmospheric scattering properties. We use the recently updated TROPOMI version 2.02 retrieval from the Netherlands Institute for Space Research (Lorente et al., 2021; <http://www.tropomi.eu/data-products/methane>), filtering out low-quality retrievals ('qa_value' < 0.5) and surfaces above 2 km where the stratospheric contribution to the column is large (Shen et al., 2022). We further adopt the 'blended albedo' filter suggested in Lorente et al (2021) to remove snow- or ice-covered scenes identified by blended albedo exceeding 0.8 from October to April.

120 Global mean bias in the TROPOMI observations is inconsequential for regional inversions because it can be incorporated in the boundary conditions, and random error (precision) is effectively reduced through the large number of observations (Fig. 1). More problematic is spatially variable bias, which corrupts the information on methane concentration gradients used to optimize emissions in the inversion. This variable bias typically arises from aliasing of surface spectral features into the XCH_4 retrieval. Lorente et al. (2021) estimated a variable bias of 5.6 ppb for the TROPOMI XCH_4 full-physics retrieval as the spatial standard deviation of the mean difference with ground-based methane observations from the Total Carbon Column Observing Network (TCCON; Wunch et al., 2011). This is below the threshold requirement of 10 ppb recommended by Buchwitz et al. (2015) for use of satellite data in regional inversions. However, the TCCON network is sparse and includes no sites in China.

130 *Qu et al.* (2021) conducted a more thorough worldwide analysis of variable bias in the
TROPOMI version 1.03 data (*Hu et al.*, 2018) by using the GOSAT observations as reference on
a $4^{\circ} \times 5^{\circ}$ grid. GOSAT is much less subject to retrieval artifacts because of its higher spectral
resolution and its use of the CO₂ proxy retrieval method in the 1.65 μm absorption band (*Parker*
et al., 2020). *Qu et al.* (2021) found TROPOMI variable biases typically in the range 9-13 ppb
but exceeding 20 ppb for some regions. Repeating this analysis for our East Asia domain with
TROPOMI version 2.02 (*Lorente et al.*, 2021) on the $0.25^{\circ} \times 0.3125^{\circ}$ grid, we find a mean
TROPOMI-GOSAT difference of -9.9 ± 17.6 ppb (Fig. 2a). The mean difference is largely driven
by TROPOMI values below 1830 ppb at high latitudes (Fig. 1), likely reflecting snow-covered
140 surfaces that are not successfully removed by the blended albedo filter. The standard deviation of
the difference (measure of variable bias) is relatively high in part due to the high spatial
resolution in our analysis, which also means that a higher bias threshold is acceptable because
methane enhancements are larger. Here we exclude TROPOMI observations that show
discrepancies larger than 20 ppb compared to GOSAT. The mean TROPOMI-GOSAT difference
after these outlying data have been excluded is -3.6 ± 9.1 ppb with no evident regional structure
(Fig. 2b).

Fig. 1 shows the mean TROPOMI observations for 2019 retained in our analysis on the
 $0.25^{\circ} \times 0.3125^{\circ}$ grid, along with the number of observations in each grid cell. We assimilate $m =$
5907939 TROPOMI retrievals over the inversion domain. There are few observations in western
China and no observations at all in Tibet because we have excluded locations with surface
150 altitude above 2 km following *Shen et al.* (2022).

2.2 Prior emissions

Fig. 3 shows the prior estimates of emissions from different sectors over the inversion domain
and Table 1 gives national totals for China. Anthropogenic emissions for China are from the
latest 2014 national governmental report to the UNFCCC (*UNFCCC*, 2020). Emissions from
coal and oil/gas exploitation are spatially allocated to the $0.25^{\circ} \times 0.3125^{\circ}$ GEOS-Chem grid using
infrastructure information compiled by the Global Fuel Exploitation Inventory (GFEI v2;
Scarpelli et al., 2022). This includes bottom-up information from *Sheng et al.* (2019) for the
160 distribution of China's coal emissions. Other anthropogenic sources are spatially allocated using
the EDGAR v4.3.2 inventory. Anthropogenic emissions outside of China are from GFEI v2 for
fuel exploitation and from EDGAR v4.3.2 for other sectors. *Wolf et al.* (2017) produced an
alternative global gridded inventory for livestock emissions but we find that it is too uniform
over China, as *Scarpelli et al.* (2020a) previously found over Mexico, because they use livestock
numbers resolved only by province and distribute them over all grasslands and shrublands. All
anthropogenic emissions are assumed to be aseasonal, except for manure management for which
we apply temperature-dependent corrections following *Maasackers et al.*, (2016) and rice
paddies for which we apply seasonal corrections derived from a biogeochemical model (*B.*
Zhang et al., 2016).

170 Wetland emissions are monthly means for 2019 on a $0.5^{\circ} \times 0.5^{\circ}$ grid from the nine-member high-
performance subset of the WetCHARTs v1.3.1 inventory ensemble that best fits global GOSAT
inversions (*Ma et al.*, 2021). Other natural sources include daily open-fire emissions from the
Global Fire Emissions Database version 4s (GFED4s; *van der Werf et al.*, 2017), termite

emissions from *Fung et al* (1991), and geological seepage emissions from *Etioppe et al* (2019) scaled to a global magnitude of 2 Tg a⁻¹ following *Hmiel et al* (2020).

2.3 GEOS-Chem chemical transport model

180 A nested version of the GEOS-Chem chemical transport model (13.0.0; <https://doi.org/10.5281/zenodo.4618180>) is used as the forward model in the inversion to relate methane emissions to atmospheric observations. The model is driven by GEOS-FP reanalysis meteorological fields with 0.25° × 0.3125° spatial resolution and 3-hour temporal resolution (1-h for mixing depths and surface fields) from the NASA Global Modeling and Assimilation Office (*Lucchesi, 2013*). We conduct GEOS-Chem model simulations at 0.25° × 0.3125° resolution over the study domain of Fig. 1 for 2019. The nested version of GEOS-Chem is similar to that used in previous regional inversions of TROPOMI observations (*Y. Zhang et al., 2020; Shen et al., 2021*) and uses 3-hour dynamic boundary conditions from a global GEOS-Chem simulation at 2° × 2.5° resolution for 2019 with posterior methane emissions optimized by TROPOMI
190 observations (*Qu et al., 2021*). The global simulation includes methane sinks from atmospheric oxidation and uptake by soils, but these are inconsequential in the nested version because the ventilation time scale for the nested domain is much shorter than the methane lifetime. We convolve the GEOS-Chem vertical profiles of methane dry mixing ratios with the TROPOMI averaging kernel vectors and prior vertical profiles (*Varon et al., 2022*) to obtain the model simulation of XCH₄ for comparison to the TROPOMI observations in the inversion.

Bias in boundary conditions is critical to avoid as it would propagate to biases in the inversion. We initialize our global GEOS-Chem simulation used to define boundary conditions so that it matches the global mean of TROPOMI observations for January 1-10, 2019. Subsequent
200 simulation for 2019 using the TROPOMI-optimized emissions from *Qu et al. (2021)* avoids systematic drift of the simulation from the TROPOMI observations. To further avoid bias we optimize the boundary conditions on each side of our domain (north, south, west, and east) and for each season as part of the inversion (Table S1).

2.4. Analytical inversion

The state vector \mathbf{x} to be optimized in the inversion includes spatially resolved emissions within the inversion domain and seasonal boundary conditions. We could technically carry out the inversion on the 0.25° × 0.3125° model grid, but satellite observations do not have sufficient information to constrain emissions in such detail everywhere; attempting to do so would
210 introduce large smoothing errors (*Wecht et al., 2014; Turner and Jacob, 2015*). We instead use the Gaussian mixture model (GMM) of *Turner and Jacob (2015)* to define emission patterns that can be effectively constrained by the TROPOMI observations as informed by the prior estimates. The GMM functions are selected with the goal of retaining native resolution for strong localized source features while merging weak source regions. Specifically, we project methane emissions at 0.25° × 0.3125° resolution onto 600 Gaussian functions. Each of the functions is uniquely characterized by a mean location, spatial standard deviation, and emission magnitude; these parameters are estimated using similarity vectors on the 0.25° × 0.3125° grid that incorporate information of spatial proximity (longitude and latitude), and the prior emission patterns by sector (Fig. 3). The inversion optimizes the emissions for each Gaussian along with 16 boundary
220 conditions (four seasons × four boundaries) for a total of $n = 616$ elements.

We perform the inversion with lognormal error probability density functions (pdfs) for prior emissions (*Maasackers et al.*, 2019; *Lu et al.*, 2022), which enforces positivity of the solution and better captures the high tail of the frequency distribution of emissions than a normal error pdf. High-tailed emissions have been observed for the oil/gas (*Yuan et al.*, 2015; *Zavala-Araiza et al.*, 2015; *Lyon et al.*, 2015; *Alvarez et al.*, 2018), coal (*Sadavarte et al.*, 2021), waste (*Maasackers et al.*, 2022), and livestock sectors (*Duren et al.*, 2019). In this section we first describe the inversion procedure with normal error pdfs and then explain the transformation to lognormal error pdfs.

230 Bayesian inference of the optimal posterior estimate for the state vector \mathbf{x} assuming normal error pdfs involves minimization of the cost function $J(\mathbf{x})$ (Brasseur and Jacob, 2017):

$$J(\mathbf{x}) = (\mathbf{x} - \mathbf{x}_a)^T \mathbf{S}_a^{-1} (\mathbf{x} - \mathbf{x}_a) + \gamma (\mathbf{y} - \mathbf{K}\mathbf{x})^T \mathbf{S}_o^{-1} (\mathbf{y} - \mathbf{K}\mathbf{x}) \quad (1)$$

where \mathbf{x} ($n \times 1$) is the n -dimensional state vector to be optimized, \mathbf{x}_a ($n \times 1$) is its prior estimate, and \mathbf{y} ($m \times 1$) is the m -dimensional vector of TROPOMI observations ($m = 5907939$). \mathbf{S}_a ($n \times n$) is the prior error covariance matrix and \mathbf{S}_o ($m \times m$) is the observational error covariance matrix. $\mathbf{K} = \partial \mathbf{y} / \partial \mathbf{x}$ ($m \times n$) is the Jacobian matrix that describes the sensitivity of observations to the state vector as represented by GEOS-Chem, and γ is a regularization factor to avoid over/underfit to observations. γ is needed because the observational error covariance matrix can only be roughly estimated and is assumed here to be diagonal for lack of better information and convenience of computation. The relationship between methane emissions and concentrations in the nested
240 GEOS-Chem simulation is linear, so that \mathbf{K} defines the forward model for the purpose of the inversion.

Prior error standard deviations for emission state vector elements (square roots of diagonal terms of \mathbf{S}_a) are assumed to be 50% for the specification of normal error pdfs and a factor of 2 for the specification of log-normal error pdfs. Observational error standard deviations (square roots of diagonal terms of \mathbf{S}_o) include contributions from instrument error, retrieval error, representation error, and forward model error. We calculate the sum of these errors using the residual error method (*Heald et al.*, 2004) on the basis of the XCH_4 differences $\Delta = \mathbf{y} - \mathbf{y}_{\text{GEOS-Chem,prior}}$ for individual $0.25^\circ \times 0.3125^\circ$ grid cells between individual TROPOMI observations and the GEOS-
250 Chem simulation with prior emissions. The temporal mean 2019 difference $\bar{\Delta} = \overline{\mathbf{y} - \mathbf{y}_{\text{GEOS-Chem,prior}}}$ for each grid cell is to be corrected in the inversion while the standard deviation of the residual difference $\Delta - \bar{\Delta}$ is taken as the observational error standard deviation, adjusted up to a minimum value of 10 ppb following *Maasackers et al.* (2019) if necessary (10.4% of the retrievals). The resulting observational error standard deviation averages 13.4 ppb, which agrees closely with previous TROPOMI inverse analyses and is mostly due to retrieval error (*Shen et al.*, 2021; *Qu et al.*, 2021).

Minimization of the cost function in Eq. (1) can be solved analytically at $\nabla_{\mathbf{x}} J(\mathbf{x}) = 0$ following *Rodgers* (2000), to obtain the optimal posterior estimate $\hat{\mathbf{x}}$:

$$\hat{\mathbf{x}} = \mathbf{x}_a + \gamma \mathbf{S}_a \mathbf{K}^T (\gamma \mathbf{K} \mathbf{S}_a \mathbf{K}^T + \mathbf{S}_o)^{-1} (\mathbf{y} - \mathbf{K} \mathbf{x}_a) \quad (2)$$

260 with posterior error covariance matrix $\hat{\mathbf{S}}$:

$$\hat{\mathbf{S}} = (\gamma \mathbf{K}^T \mathbf{S}_o^{-1} \mathbf{K} + \mathbf{S}_a^{-1})^{-1} \quad (3)$$

The averaging kernel matrix \mathbf{A} quantifies the sensitivity of the solution to the true value:

$$\mathbf{A} = \frac{\partial \hat{\mathbf{x}}}{\partial \mathbf{x}} = \mathbf{I}_n - \hat{\mathbf{S}}\mathbf{S}_a^{-1} \quad (4)$$

where \mathbf{I}_n is the identity matrix. The trace of \mathbf{A} measures the number of independent pieces of information on the state vector \mathbf{x} obtained from the observations, and is often referred to as the degrees of freedom for signal (DOFS).

The optimal value of γ can be determined following *Lu et al. (2021)* so that the sum of state vector terms in the posterior estimate of the cost function, $J_a(\hat{\mathbf{x}}) = (\hat{\mathbf{x}} - \mathbf{x}_a)^T \mathbf{S}_a^{-1} (\hat{\mathbf{x}} - \mathbf{x}_a)$ has value of $\sim n \pm \sqrt{2n}$, which is the expected value (± 1 standard deviation) from the Chi-square distribution with n degrees of freedom. We find in this manner an optimal γ value of 0.015 as the best fit for our TROPOMI inversion. This is smaller than a previous regional TROPOMI inversion at $0.25^\circ \times 0.3125^\circ$ resolution ($\gamma=0.25$ in *Shen et al., 2021*) because of the much larger number of observations per state vector element (m/n) in our work. We also conducted sensitivity inversions using $\gamma = 0.005$ and 0.03 ns as described in Sect. 2.6.

Analytical solution requires explicit construction of the Jacobian matrix \mathbf{K} . We construct \mathbf{K} column by column, by perturbing individual elements x_i of the state vector independently and running GEOS-Chem forward model simulations to obtain the columns $\partial y / \partial x_i$. These simulations are readily achievable with massively parallel computing. Sparse matrix algebra is applied wherever possible in matrix calculations, making use of the diagonal structure of the error covariance matrices \mathbf{S}_a and \mathbf{S}_o .

Assuming normal errors for prior emissions may lead to unphysical negative posterior emissions (*Miller et al., 2014*) and fails to model the high tail of emission pdfs. We instead assume lognormal errors. Specifically we optimize $\ln(\mathbf{x})$ instead of \mathbf{x} , with the prior errors on $\ln(\mathbf{x})$ following a Gaussian distribution. The optimization problem is then nonlinear and needs to be solved iteratively. We do this by updating the Jacobian matrix $\mathbf{K}'_N = \frac{\partial \mathbf{y}}{\partial \ln(\mathbf{x})} = \mathbf{x} \frac{\partial \mathbf{y}}{\partial \mathbf{x}}$ at each iteration N , which can be immediately derived from the original Jacobian matrix $\mathbf{K} = \frac{\partial \mathbf{y}}{\partial \mathbf{x}}$ in Eq. (1). We iteratively approach the solution using the Levenberg-Marquardt method (*Rodgers, 2000*):

$$\mathbf{x}'_{N+1} = \mathbf{x}'_N + (\gamma \mathbf{K}'_N{}^T \mathbf{S}_o^{-1} \mathbf{K}'_N + (1+k) \mathbf{S}'_a{}^{-1})^{-1} (\gamma \mathbf{K}'_N{}^T \mathbf{S}_o^{-1} (\mathbf{y} - \mathbf{K} \mathbf{x}_N) - \mathbf{S}'_a{}^{-1} (\mathbf{x}'_N - \mathbf{x}'_a)) \quad (5)$$

where $\mathbf{x}' = \ln(\mathbf{x})$ and $\mathbf{x}'_a = \ln(\mathbf{x}_a)$. k is a coefficient for the iterative approach and we use $k = 10$ following *Lu et al (2022)*. \mathbf{S}'_a is the prior error covariance matrix (with diagonal elements s'_a) in log space. We assume a geometric standard deviation factor (σ_g) of 2 for the lognormally distributed errors in \mathbf{x} and construct the \mathbf{S}'_a matrix following $\sqrt{s'_a} = \ln(\sigma_g)$ (*Kirkwood, 1979; Limpert et al., 2001*).

We iterate on Eq. (5) until the maximum difference in state vector elements between two consecutive iterations (\mathbf{x}'_N and \mathbf{x}'_{N+1}) is smaller than 0.5%, at which point we adopt $\hat{\mathbf{x}}' = \mathbf{x}'_{N+1}$ as the best posterior estimate. The posterior error covariances and averaging kernel matrix on the log solution are then readily obtained by replacing \mathbf{S}_a and \mathbf{K} with \mathbf{S}'_a and \mathbf{K}' in Eq. (3). The optimal posterior estimate in log space is for the median of emission but not for the mean; mean emissions are however necessary for spatial aggregation and sectoral attribution purposes. Here

we make use of the posterior error covariance matrix from Eq. (3) to infer the mean emissions from the median following the lognormal distribution statistics $x_{mean} = x_{median} e^{\hat{s}^T/2}$, where \hat{s}^T is the diagonal element of the posterior error covariance matrix in log space corresponding to that state vector element. The normal error assumption is retained for the boundary conditions elements of the state vector, with a prior error standard deviation of 10 ppb.

2.5 Sectoral attribution of posterior emissions

The posterior estimate of methane emissions for the GMM state vector can be readily mapped on the $0.25^\circ \times 0.3125^\circ$ grid by summation of the GMM elements, but it is also of interest to aggregate it spatially for inferring national totals including by source sector. This reduction in state vector dimension is readily done while preserving the information from the posterior error covariance matrix by using a summation matrix \mathbf{W} to represent the linear transformation from the full state vector ($n \times 1$) to the reduced state vector. The posterior estimate of the reduced state vector (\mathbf{x}_{red}) is computed as

$$\hat{\mathbf{x}}_{red} = \mathbf{W}\hat{\mathbf{x}} \quad (6)$$

and the posterior error covariance and averaging kernel matrices are then given by

$$\hat{\mathbf{S}}_{red} = \mathbf{W}\hat{\mathbf{S}}\mathbf{W}^T \quad (7)$$

$$\mathbf{A}_{red} = \mathbf{W}\mathbf{A}\mathbf{W}^* \quad (8)$$

where $\mathbf{W}^* = (\mathbf{W}^T\mathbf{W})^{-1}\mathbf{W}^T$ is the Moore-Penrose pseudo inverse (Calisesi *et al.*, 2005).

2.6 Error characterization and inversion ensemble

The sections above describe our base inversion with solution defined by $(\hat{\mathbf{x}}, \hat{\mathbf{S}})$. By using the regularization factor γ , we prevent overfit to the observations and therefore $\hat{\mathbf{S}}$ is a fair representation of the uncertainty within our choice of inversion parameters. However, there is uncertainty in these parameters, and we therefore perform an ensemble of sensitivity inversions with different choices. The sensitivity inversions include (1) using $\ln(1.5)$, and $\ln(2.5)$ for the prior error standard deviations instead of $\ln(2)$; (2) using 0.005 and 0.03 for the regularization factor γ instead of 0.015; and (3) using 5 and 20 ppb for the prior error standard deviation in the boundary condition elements of the state vector instead of 10 ppb. We also perform sensitivity inversions assuming normally distributed errors with prior error standard deviation $\sqrt{s_a}=50\%$. Combination of these perturbations to our inversion framework generates 36 members in the inversion ensemble. The uncertainty in posterior estimates reported here is taken as the greater of the range of solutions given by the inversion ensemble and the 2-sigma error inferred from the diagonal of $\hat{\mathbf{S}}$, and is generally determined by the ensemble (Fig. S1).

3. Results

3.1 Evaluation of posterior emission estimates

Fig. 4 compares the prior and posterior estimates of emissions mapped on the $0.25^\circ \times 0.3125^\circ$ grid. It also shows the averaging kernel sensitivities (diagonal terms of the averaging kernel

340 matrix), which measure the ability of TROPOMI observations to determine the posterior solution independently of the prior estimate (0=not at all; 1=perfectly). High averaging kernel sensitivities reflect a combination of high observation density and large prior emissions. We achieve high sensitivities to observations in major source regions, with 167 independent pieces of information (DOFS) out of the 600 Gaussian state vector elements.

Comparison of GEOS-Chem simulations using posterior versus prior emissions indicates an improved ability of the posterior emissions to fit the TROPOMI observations (Fig. 1). The mean bias over the inversion domain decreases from 7.8 to 0.4 ppb while the RMSE decreases from 16.8 to 13.6 ppb. The inversion effectively corrects the mean bias from using the prior emissions. The ability to decrease the RMSE is limited by the retrieval error on individual observations.

350 We independently evaluate the posterior estimate by comparison to *in situ* surface observations from the GLOBALVIEWplus CH₄ ObsPack v4.0 database compiled by the National Oceanic and Atmospheric Administration (NOAA) Global Monitoring Laboratory (*Schuldt et al.*, 2021). There are five sites in East Asia in 2019, all in relatively remote locations and with near-weekly sampling schedule (Fig. 5 and Table S2). The mean GEOS-Chem model bias across the five sites is -4.1 ± 9.5 ppb using prior emissions and -3.8 ± 4.7 ppb using posterior emissions. There is little decrease in the mean bias, which is consistent with the mean bias of -3.4 ppb for TROPOMI relative to TCCON (*Lorente et al.*, 2021) and implies that both the prior and posterior simulations are effectively unbiased in the mean. The factor of 2 lower standard deviation in the posterior simulation indicates a better fit to observations. The RMSE for individual observations decreases only slightly from 23.7 ppb to 20.8 ppb because it is limited by the forward model transport error, previously estimated by *Lu et al.*, (2021) at 20 ppb for the GLOBALVIEWplus CH₄ ObsPack 360 database using the residual error method. The model transport error is larger for surface than satellite observations because the amplitude of variability is larger and includes uncertainties in boundary layer vertical mixing.

Qu et al (2021) previously reported overcorrections and inconsistencies with respect to GOSAT in their global TROPOMI inversion results over southeastern China. They attributed the problem to spatial overlap of coal and rice emissions, and to seasonal cloudiness correlated with the peak in rice emissions. We have more confidence in our results for several reasons. First, our higher spatial resolution compared to the $2^\circ \times 2.5^\circ$ of *Qu et al* (2021) allows better separation of coal and rice emissions. Second, we use an improved spatial distribution of coal emissions (*Sheng et al.*, 370 2019) compared to the EDGAR v4.3.2 inventory in *Qu et al.* (2021). Third, we use version 2.02 of the TROPOMI retrieval with additional filters, and exclude data inconsistent with GOSAT (Fig. 2), whereas *Qu et al.* (2021) used TROPOMI v1.03 data with quality flags but no other filtering. Our results show higher averaging kernel sensitivities over southeastern China than *Qu et al.* (2021) and no overcorrections (Fig. 1).

3.2 National and sectoral emissions for China

Table 1 compiles the total national and sectoral posterior emissions for China. Sectoral attribution assumes that the posterior/prior emission ratios for a given $0.25^\circ \times 0.3125^\circ$ grid cell (Fig. 4) apply equally to all prior emission sectors within that grid cell. Posterior estimates of total, anthropogenic, and natural emissions for China are 70.0 (61.6-79.9), 65.0 (57.7-68.4), and 380 5.0 (3.9-11.6) Tg a⁻¹, respectively, where the parentheses indicate the uncertainty range in the inversion solution as described in Sect. 2.6. The averaging kernel sensitivities for the national total and anthropogenic posterior emission estimates are 0.91, indicating that these estimates are

largely determined by the TROPOMI observations with little influence from the prior estimate. Our best posterior estimate of 65 Tg a⁻¹ for Chinese anthropogenic emissions is 21% higher than the 2014 value of 53.6 Tg a⁻¹ reported by the Chinese government to the UNFCCC, and the range of our inversion results gives us high confidence that the reported emissions are too low.

Our ability to separate the contributions from different sectors to the posterior emission estimates for China can be evaluated by examining the error correlations in the reduced posterior error covariance matrix (Sect. 2.5), as shown in Fig. 6. We find that landfills and wastewater treatment cannot be effectively separated in the posterior solution (posterior error correlation coefficient $r = 0.95$), because they have similar spatial distributions associated with population (Fig. 3), and we thus group them as a single waste sector for further analysis. The ‘Other’ sector, which is mostly associated with urban emissions, also has strong error correlations with waste ($r = 0.66-0.75$). Other sectors can be successfully separated, as shown by the posterior error correlations in Fig. 6. We find that most of the posterior error correlation coefficients between sectors are lower than 0.2. For example, there is little error correlation ($r = -0.2$ to 0.1) between coal and other sectors. The global TROPOMI inversion by *Qu et al* (2021) found it difficult to separate emissions between coal and rice paddies, but here we find a low error correlation of -0.04 that reflects our much higher spatial resolution. The main natural emission sector is wetlands, which is effectively separated from all other sectors except rice ($r = 0.29$).

We can now attribute the 21% underestimate of anthropogenic emissions in the Chinese government report to the UNFCCC, as given in Table 1. We find large upward corrections in emissions from oil (+147%), gas (+61%), livestock (+37%), rice paddies (+34%), and waste (+41%), but a downward correction in coal emissions (-15%). Averaging kernel sensitivities for all anthropogenic sectors are high (0.71-0.91), indicating strong constraints from the observations. An exception is the gas sector (0.31), for which emissions are relatively small. The uncertainty ranges of the inversion results for the different sectors are small, indicating an insensitivity to different inversion assumptions and high confidence in the posterior sectoral emissions in the base inversion.

The inversion returns a larger estimate of 5.0 (3.9-11.6) Tg a⁻¹ for natural sources relative to 3.2 Tg a⁻¹ in the prior estimate, mainly driven by increased contributions from wetlands (+1.1 Tg a⁻¹) and termites (+0.5 Tg a⁻¹). Averaging kernel sensitivity for wetlands is moderately high (0.61) but low for the other small natural sources.

The base inversion assuming a lognormal error distribution for prior emissions returns larger posterior Chinese emissions from all sectors relative to a normal error assumption, as would be expected from the asymmetry of the lognormal function. The largest differences are for the oil and gas sectors, where the sensitivity inversion assuming a normal error distribution yields posterior estimates respectively 22% and 21% lower than the base inversion. The oil and gas sectors are particularly high-tailed in their frequency distributions of emissions (*Zavala-Araiza et al.*, 2015; *Lyon et al.*, 2015; *Brandt et al.*, 2016; *Alvarez et al.*, 2018).

4. Discussion

By using the official Chinese inventory reported to the UNFCCC as prior estimate of methane emissions, our inversion can usefully evaluate that inventory and guide its improvement. Here

we discuss the significance and implications of our results for different sectors, placing them in the context of previous literature, and we identify specific issues requiring further work.

430 Fig. 7 compiles the total and sectoral anthropogenic emissions in China reported by top-down and bottom-up studies for the past decade. Our total posterior emission estimate of 65 (57.7-68.4) Tg a⁻¹ is consistent with the EDGAR inventories but this reflects canceling differences for individual sectors as shown in the bottom panel. We estimate higher national total emissions than *Peng et al* (2016), driven by their much smaller rice and waste emissions. Our estimate is higher than the best estimates from previous top-down studies (43-62 Tg a⁻¹), which used EDGAR prior estimates for spatial distribution, and were conducted at much coarser resolutions (2°×2.5°-4°×5° versus 0.25°×0.3125°) and with much sparser observations (GOSAT versus TROPOMI) than ours. *Deng et al* (2022) compiled results from 11 GOSAT inversions for 2010-2017 using Chinese UNFCCC totals as prior estimate and showing a range of 40-62 Tg a⁻¹. Although the studies are from different years, *Lu et al.* (2021) and *Y. Zhang et al.* (2021) reported an increasing Chinese emission trend of 0.4 Tg a⁻¹ from inversion of 2010-2018 GOSAT observations, which would only make a small contribution to the differences. The lower emissions in the previous top-down studies are mostly driven by downward revision of coal emissions relative to their prior estimates, and we find such a decrease too but not to the same extent. Our inversion uses an improved prior estimate of the distribution of coal emissions in China with much larger contribution from southern China (*Sheng et al.*, 2019), so that some of the previous corrections attributed to rice agriculture might reflect coal emissions instead. Another striking difference in our work relative to others is the much higher livestock emissions. We discuss the coal, oil/gas, livestock, and waste sectors in more detail below.

4.1 Coal

450 Our downward correction of coal emissions compared to the UNFCCC report is driven by both Shanxi province and southwestern China, which are the two largest coal producing regions in China (*Zhu et al.*, 2017). This could reflect (1) overestimate of EFs in the UNFCCC report, (2) under-accounting of surface mines, and (3) increasing coal methane utilization. With regard to (1), many high methane-content coal mines with inefficient coal production have been closed in the past decade (*Wang et al.*, 2020). Coal production has shifted from southern and eastern China to northwestern China (including Shanxi) with abundant coal reserves and where methane content is relatively low (*Gao et al.*, 2021; *Liu et al.*, 2021). With regard to (2), a previous study (*Gao et al.*, 2021) indicated an underestimated share of surface mining in the UNFCCC report for China. The methane emission intensity of surface mining is ten times lower than underground mining (*Palmer et al.*, 2021). With regard to (3), coal mine methane (CMM) utilization in China has greatly increased in the past decade (*Y. Lu et al.*, 2021).

460 However, uncertainty in the spatial distribution of coal emissions remains a major obstacle for top-down studies. Different bottom-up inventories are inconsistent in their estimates of the number of mines in China (e.g., 324 in EDGAR v4.2, 4243 in EDGAR v4.3.2, and 10963 in *Sheng et al.*, 2019). Mine closures and regional shifts in coal production may also be difficult to track (*Gao et al.*, 2021). New satellite observations of methane plumes from individual point sources could provide important new information for geolocation and quantification of emissions from coal mines, as shown for the Shanxi province by *Guanter et al.* (2021) and *Sánchez-García et al.* (2022).

4.2 Oil/gas

470 Our posterior estimate of oil/gas emissions is higher than the UNFCCC report and *Peng et al* (2016), but lower than EDGAR v4.3.2 and v6. The previous top-down estimates in Fig. 7 range from 0.7 Tg a⁻¹ by *Lu et al* (2021) to 5.5 Tg a⁻¹ by *Miller et al* (2019), and our estimate is in mid-range. *Scarpelli et al* (2022) found that the oil/gas emissions from *Lu et al* (2021) were heavily influenced by the low GFEI v1 inventory (*Scarpelli et al.*, 2020b) used as their prior estimate. The high emissions in *Miller et al* (2019) could reflect their use of the EDGAR v4.2 inventory as prior estimate with spuriously high emissions from pipelines (*Scarpelli et al.*, 2020b).

480 We find that the oil sector has the largest relative upward correction to the UNFCCC inventory (+147%) among all sectors. The correction might be attributed to methane leakage from oil extraction not fully accounted for in the UNFCCC report (*Rutherford et al.*, 2021; *Deng et al.*, 2022). *Lauvaux et al* (2022) used 2019-2020 TROPOMI observations to identify a number of ultra-emitters (>25 tons h⁻¹ on the 5.5×7 km² grid) from oil production fields; their identified ultra-emitters in China are consistent with the locations where we find large oil upward adjustments.

Gas emissions for China in the UNFCCC report (0.18 Tg a⁻¹) are dominated by distribution (0.125 Tg a⁻¹) with only small contributions from production (0.03 Tg a⁻¹) and transmission (0.025 Tg a⁻¹). This is in part because of low EFs from production, and in part because a large fraction of the gas used in China is imported. The assumed EF for gas production in the UNFCCC report is 1.3×10⁻¹⁰ Gg per m³ of gas production, much lower than in the IPCC (2006) EF guidelines (lower-end value of 3.8×10⁻¹⁰ Gg per m³ of gas production for developed countries). 42% of the gas used in China in 2019 was imported (EIA, 2020).

490 Our inversion returns a posterior emission for the gas sector of 0.29 Tg a⁻¹ including 0.16 Tg a⁻¹ from distribution, 0.07 Tg a⁻¹ from production, and 0.06 Tg a⁻¹ from transmission. However, the averaging kernel sensitivity is low (0.3) and the distribution subsector is difficult to disentangle from the waste sector because it is mostly urban. *Alvarez et al* (2012) suggested that the life-cycle loss rate from gas production should be less than 3.2% for a coal-to-gas transition to be of climate benefit. Our posterior estimate indicates a loss rate of 1.7 (1.3-1.9) % for China, assuming 92% methane gas by volume (*Scarpelli et al.*, 2022).

500 China's gas industry has entered a rapid development stage driven by the domestic coal-to-gas transition policy (*Qin et al.*, 2018); China's gas production in 2019 was 42% higher than in the 2014 year of the UNFCCC inventory (EIA, 2020). The small loss rate suggests that the transition will be beneficial for climate, but is somewhat misleading because of the large fraction of imported gas. 25% of that imported gas is from Turkmenistan (EIA, 2020), where emissions from gas production are exceedingly high (*Varon et al.*, 2019; *Ikakulis-Loixalte et al.*, 2022; *Lauvaux et al.*, 2022). A more complete accounting of the loss rate in China from gas production would factor in the effect of international trade.

4.3 Livestock

510 Our estimate of Chinese livestock emissions is higher than any previous study (Fig. 7). This is because our inversion corrects livestock emissions upward in northwestern and northeastern China, where existing bottom-up inventories show weak emissions (*Lin et al.*, 2021). Previous GOSAT inversions had poor observational coverage over these regions (Fig. 5 in *Qu et al.*, 2021), and their inversion solutions hence cannot depart sufficiently from the low bottom-up

inventories used as prior estimates. However, TROPOMI observations provide strong constraints as illustrated by the high averaging kernel values (Fig. 3).

4.4 Waste

We estimate higher waste emissions than the 2010 *Peng et al* (2016) inventory and the 2014 UNFCCC report, and we attribute this in part to the rapid development of wastewater treatment in China. China has enacted major policies on water pollution prevention since 2014 (*Xu et al.*, 2020), including new standards for sewage discharge (*Han et al.*, 2016). The number of wastewater treatment plants increased by 44% from 2014 to 2019 (*Xu et al.*, 2020). Solid waste generation has also increased in the past decade (*Sheng et al.*, 2021) but an increasing fraction is
520 incinerated rather than landfilled (*Liu et al.*, 2021).

5. Conclusions

We estimated 2019 methane emissions in China by high-resolution inversion of TROPOMI satellite observations. Our inversion uses as prior estimate the Chinese national inventory reported to the UNFCCC so that our results are directly relevant for evaluating and improving that inventory.

Our inversion uses an analytical solution to the Bayesian inference of methane emissions from the TROPOMI observations, providing closed-form statistics on posterior errors and information content as part of the solution. It optimizes a 600-member Gaussian mixture model (GMM) of
530 emissions, in which concentrated source regions are quantified at up to $0.25^{\circ} \times 0.3125^{\circ}$ ($\approx 25 \times 25$ km²) resolution while regions with weak emissions are spatially aggregated. We assume lognormal error distributions for the prior emissions, which allows better representation of the high-tailed component. The Jacobian sensitivity matrix constructed for our analytical solution enables immediate generation of an inversion ensemble to explore the dependence of the solution on uncertainties in inversion parameters. This ensemble is combined with the posterior error covariance matrix of the base inversion to provide a conservative estimate of errors on inferred emissions including from different sectors. Independent evaluation of inversion results with surface sites from the NOAA GLOBALVIEWplus CH₄ ObsPack v4.0 database shows significant improvement in the ability to fit the observations.

540 We estimate from the inversion a total emission for China of 70.0 (61.6-79.9) Tg a⁻¹, where the parentheses indicate the uncertainty ranges. Total anthropogenic emission for China is 65.0 (57.7–68.4) Tg a⁻¹ including 16.6 (15.6-17.6) Tg a⁻¹ from coal, 2.3 (1.8-2.5) Tg a⁻¹ from oil, 0.29 (0.23-0.32) Tg a⁻¹ from gas, 17.8 (15.1-21.0) Tg a⁻¹ from livestock, 9.3 (8.2-9.9) Tg a⁻¹ from waste, 11.9 (10.7-12.7) Tg a⁻¹ from rice paddies, and 6.7 (5.8-7.1) Tg a⁻¹ from other sources. Our inferred total anthropogenic emission for China is 21% higher than the national inventory reported by the Chinese government to the UNFCCC (53.6 Tg a⁻¹). This reflects upward corrections to emissions from oil (+147%), gas (+61%), livestock (+37%), waste (+41%), and rice paddies (+34%), and a downward correction in coal emissions (-15%).

550 Our estimate of anthropogenic Chinese emissions is at the high end of the range of past inversion studies (43-62 Tg a⁻¹) that used the much sparser GOSAT satellite observations, coarser resolution, and versions of the EDGAR inventory as prior estimates. We find in particular higher emissions from coal, livestock, and waste. The higher emission from coal may reflect our

improved accounting of sources in southern China (*Sheng et al.*, 2019) and a higher spatial resolution that allows us to better separate emissions from coal and rice paddies (*Qu et al.*, 2021). Our upward correction to livestock emissions is mostly in northwestern and northeastern China, where TROPOMI provides much denser information than was previously achievable from GOSAT. Our high estimate of emissions from waste may be driven in part by the large increase in wastewater treatment plants in China over the past decade.

560 Our upward corrections relative to the Chinese government inventory are largest for oil and gas, even though the contributions from these two sectors to total national methane emissions are still small compared to other sectors. We find high emissions from oil production in the same locations where *Lauvaux et al.* (2022) identified ‘ultra-emitters’ in the TROPOMI data, suggesting that much of these emissions originate from malfunctioning or poorly operated equipment. Most of the gas emissions in China are from distribution, reflecting low emission factors from gas production but also a large share of imported gas. Emission from gas may increase in the future as China undergoes a coal-to-gas transition in energy policy (*Qin et al.*, 2018) with increasing domestic gas production. We derive a life-cycle loss rate of 1.7 (1.3-1.9) % from gas production in China, lower than the 3.2% break-even point for a coal-to-gas transition to be beneficial for climate (*Alvarez et al.*, 2012). However, this does not account for
570 imported gas from countries such as Turkmenistan where emission per unit of gas production is exceedingly high.

580 *Acknowledgments.* This work was funded by the Climate and Clean Air Coalition (CCAC) of the United Nations Environment Programme (UNEP) and by the NASA Carbon Monitoring System.

Data availability. The TROPOMI satellite observations version 2.02 are available at <http://www.tropomi.eu/data-products/methane>; The GOSAT methane retrievals version 9.0 are available at <https://catalogue.ceda.ac.uk/uuid/18ef8247f52a4cb6a14013f8235cc1eb>; The ObsPack GLOBALVIEWplus CH4 ObsPack v4.0 data product is available at <https://gml.noaa.gov/ccgg/obspack/data.php>.

Author contributions. ZC and DJJ contributed to the study conceptualization. ZC conducted the data and modeling analysis with contributions from HN, MPS, AL, DJV, XL, LS, ZQ, EP, and XYY. ZC and DJJ wrote the paper with input from all authors.

Competing interests. The authors declare that they have no conflict of interest.

590

References

- Alexe, M., Bergamaschi, P., Segers, A., Detmers, R., Butz, A., Hasekamp, O., Guerlet, S., Parker, R., Boesch, H., Frankenberg, C. and Scheepmaker, R.A.: Inverse modelling of CH₄ emissions for 2010–2011 using different satellite retrieval products from GOSAT and SCIAMACHY. *Atmos. Chem. Phys.*, 15(1), 113-133, <https://doi.org/10.5194/acp-15-113-2015>, 2015.
- Alvarez, R.A., Pacala, S.W., Winebrake, J.J., Chameides, W.L. and Hamburg, S.P.: Greater focus needed on methane leakage from natural gas infrastructure. *Proc. Natl. Acad. Sci. U.S.A.*, 109(17), 6435-6440, <https://doi.org/10.1073/pnas.1202407109>, 2012.
- 600 Alvarez, R.A., Zavala-Araiza, D., Lyon, D.R., Allen, D.T., Barkley, Z.R., Brandt, A.R., Davis, K.J., Herndon, S.C., Jacob, D.J., Karion, A. and Kort, E.A.: Assessment of methane emissions from the US oil and gas supply chain. *Science*, 361(6398), 186-188, <https://doi.org/10.1126/science.aar7204>, 2018.
- Bergamaschi, P., Houweling, S., Segers, A., Krol, M., Frankenberg, C., Scheepmaker, R.A., Dlugokencky, E., Wofsy, S.C., Kort, E.A., Sweeney, C. and Schuck, T.: Atmospheric CH₄ in the first decade of the 21st century: Inverse modeling analysis using SCIAMACHY satellite retrievals and NOAA surface measurements. *J. Geophys. Res: Atmospheres*, 118(13), 7350-7369, <https://doi.org/10.1002/jgrd.50480>, 2013.
- Brandt, A.R., G.A Heath, and D. Cooley, Methane leaks from natural gas systems follow extreme distributions, *Environ. Sci. Technol.*, 50, 12512-12520, <https://doi.org/10.1021/acs.est.6b04303>, 2016.
- 610 Brasseur, G.P. and Jacob, D.J.: Modeling of atmospheric chemistry. Cambridge University Press, <https://doi.org/10.1017/9781316544754>, 2017
- Buchwitz, M., Reuter, M., Schneising, O., Boesch, H., Guerlet, S., Dils, B., Aben, I., Armante, R., Bergamaschi, P., Blumenstock, T. and Bovensmann, H.: The Greenhouse Gas Climate Change Initiative (GHG-CCI): Comparison and quality assessment of near-surface-sensitive satellite-derived CO₂ and CH₄ global data sets. *Remote Sens. Environ.*, 162, 344-362.
- Butz, A., Guerlet, S., Hasekamp, O., Schepers, D., Galli, A., Aben, I., Frankenberg, C., Hartmann, J.M., Tran, H., Kuze, A. and Keppel-Aleks, G.: Toward accurate CO₂ and CH₄ observations from GOSAT. *Geophys. Res. Lett.*, 38(14), <https://doi.org/10.1016/j.rse.2013.04.024>, 2011.
- 620 Calisesi, Y., Soebijanta, V.T. and van Oss, R.: Regridding of remote soundings: Formulation and application to ozone profile comparison. *J. Geophys. Res: Atmospheres*, 110(D23), <https://doi.org/10.1029/2005JD006122>, 2005.
- Cheewaphongphan, P., Chatani, S. and Saigusa, N.: Exploring gaps between bottom-up and top-down emission estimates based on uncertainties in multiple emission inventories: a case study on CH₄ emissions in China. *Sustainability*, 11(7), p.2054, <https://doi.org/10.3390/su11072054>, 2019.

- 630 Crippa, M., Guizzardi, D., Solazzo, E., Muntean, M., Schaaf, E., Monforti-Ferrario, F., Banja, M., Olivier, J.G.J., Grassi, G., Rossi, S. and Vignati, E.: GHG emissions of all world countries–2021 Report. Office of the European Union, Luxembourg. doi:10.2760/173513, 2021.
- Deng, Z., Ciais, P., Tzompa-Sosa, Z. A., Saunio, M., Qiu, C., Tan, C., Sun, T., Ke, P., Cui, Y., Tanaka, K., Lin, X., Thompson, R. L., Tian, H., Yao, Y., Huang, Y., Lauerwald, R., Jain, A. K., Xu, X., Bastos, A., Sitch, S., Palmer, P. I., Lauvaux, T., d'Aspremont, A., Giron, C., Benoit, A., Poulter, B., Chang, J., Petrescu, A. M. R., Davis, S. J., Liu, Z., Grassi, G., Albergel, C., Tubiello, F. N., Perugini, L., Peters, W., and Chevallier, F.: Comparing national greenhouse gas budgets reported in UNFCCC inventories against atmospheric inversions, *Earth Syst. Sci. Data*, 14, 1639–1675, <https://doi.org/10.5194/essd-14-1639-2022>, 2022.
- 640 Duren, R.M., Thorpe, A.K., Foster, K.T., Rafiq, T., Hopkins, F.M., Yadav, V., Bue, B.D., Thompson, D.R., Conley, S., Colombi, N.K. and Frankenberg, C.: California's methane super-emitters. *Nature*, 575(7781), pp.180-184, <https://doi.org/10.1038/s41586-019-1720-3>, 2019.
- EIA: International Energy Statistics, <https://www.eia.gov/international/data/world>, 2020.
- Etiopie, G., Ciotoli, G., Schwietzke, S. and Schoell, M.: Gridded maps of geological methane emissions and their isotopic signature. *Earth Syst. Sci. Data*, 11(1), 1-22, <https://doi.org/10.5194/essd-11-1-2019>, 2019.
- Fung, I., John, J., Lerner, J., Matthews, E., Prather, M., Steele, L.P. and Fraser, P.J.: Three-dimensional model synthesis of the global methane cycle. *J. Geophys. Res: Atmospheres*, 96(D7), 13033-13065, <https://doi.org/10.1029/91JD01247>, 1991.
- 650 Gan, Y., El-Houjeiri, H.M., Badahdah, A., Lu, Z., Cai, H., Przesmitzki, S. and Wang, M.: Carbon footprint of global natural gas supplies to China. *Nat. Commun.*, 11(1), 1-9, <https://doi.org/10.1038/s41467-020-14606-4>, 2020.
- Gao, J., Guan, C., Zhang, B. and Li, K.: Decreasing methane emissions from China's coal mining with rebounded coal production. *Environ. Res. Lett.*, 16(12), p.124037, <https://doi.org/10.1088/1748-9326/ac38d8>, 2021.
- Guanter, L., Irakulis-Loitxate, I., Gorroño, J., Sánchez-García, E., Cusworth, D.H., Varon, D.J., Cogliati, S. and Colombo, R.: Mapping methane point emissions with the PRISMA spaceborne imaging spectrometer. *Remote Sens. Environ.*, 265, 112671, <https://doi.org/10.1016/j.rse.2021.112671>, 2021.
- 660 Han, D., Currell, M.J. and Cao, G.: Deep challenges for China's war on water pollution. *Environ. Pollut.*, 218, 1222-1233, <https://doi.org/10.1016/j.envpol.2016.08.078>, 2016.
- Heald, C.L., Jacob, D.J., Jones, D.B., Palmer, P.I., Logan, J.A., Streets, D.G., Sachse, G.W., Gille, J.C., Hoffman, R.N. and Nehr Korn, T.: Comparative inverse analysis of satellite (MOPITT) and aircraft (TRACE-P) observations to estimate Asian sources of carbon monoxide. *J. Geophys. Res: Atmospheres*, 109(D23), <https://doi.org/10.1029/2004JD005185>, 2004.
- Hmiel, B., Petrenko, V.V., Dyonisius, M.N., Buizert, C., Smith, A.M., Place, P.F., Harth, C., Beaudette, R., Hua, Q., Yang, B. and Vimont, I.: Preindustrial 14CH4 indicates greater

- anthropogenic fossil CH₄ emissions. *Nature*, 578(7795), 409-412, <https://doi.org/10.1038/s41586-020-1991-8>, 2020.
- 670 Houweling, S., Krol, M., Bergamaschi, P., Frankenberg, C., Dlugokencky, E. J., Morino, I., Notholt, J., Sherlock, V., Wunch, D., Beck, V., Gerbig, C., Chen, H., Kort, E. A., Röckmann, T., and Aben, I.: A multi-year methane inversion using SCIAMACHY, accounting for systematic errors using TCCON measurements, *Atmos. Chem. Phys.*, 14, 3991–4012, <https://doi.org/10.5194/acp-14-3991-2014>, 2014.
- Hu, H., Landgraf, J., Detmers, R., Borsdorff, T., Aan de Brugh, J., Aben, I., Butz, A. and Hasekamp, O.: Toward global mapping of methane with TROPOMI: First results and intersatellite comparison to GOSAT. *Geophys. Res. Lett.*, 45(8), 3682-3689, <https://doi.org/10.1002/2018GL077259>, 2018.
- 680 Irakulis-Loitxate, I., L. Guanter, J.D. Maasakkers, D. Zavala-Araiza, and I. Aben: Satellites detect abatable super-emissions in one of the world's largest methane hotspot regions, *Environ. Sci. Technol.* 56, 4, 2143–2152, <https://doi.org/10.1021/acs.est.1c04873>, 2022.
- Jacob, D. J., Turner, A. J., Maasakkers, J. D., Sheng, J., Sun, K., Liu, X., Chance, K., Aben, I., McKeever, J., and Frankenberg, C.: Satellite observations of atmospheric methane and their value for quantifying methane emissions, *Atmos. Chem. Phys.*, 16, 14371–14396, <https://doi.org/10.5194/acp-16-14371-2016>, 2016.
- Kirkwood, T.B.: Geometric means and measures of dispersion. *Biometrics*, 908-909.
- Lauvaux, T., Giron, C., Mazzolini, M., d'Aspremont, A., Duren, R., Cusworth, D., Shindell, D. and Ciais, P.: Global assessment of oil and gas methane ultra-emitters. *Science*, 375(6580), 557-561, <http://doi.org/10.1126/science.abj4351>, 2022.
- 690 Limpert, E., Stahel, W.A. and Abbt, M.: Log-normal distributions across the sciences: keys and clues. *BioScience*, 51(5), 341-352.
- Lin, X., Zhang, W., Crippa, M., Peng, S., Han, P., Zeng, N., Yu, L., and Wang, G.: A comparative study of anthropogenic CH₄ emissions over China based on the ensembles of bottom-up inventories, *Earth Syst. Sci. Data*, 13, 1073–1088, <https://doi.org/10.5194/essd-13-1073-2021>, 2021.
- Liu, G., Peng, S., Lin, X., Ciais, P., Li, X., Xi, Y., Lu, Z., Chang, J., Saunio, M., Wu, Y. and Patra, P.: Recent slowdown of anthropogenic methane emissions in China driven by stabilized coal production. *Environ. Sci. Technol. Lett.*, 8(9), 739-746, <https://doi.org/10.1021/acs.estlett.1c00463>, 2021.
- 700 Lorente, A., Borsdorff, T., Butz, A., Hasekamp, O., aan de Brugh, J., Schneider, A., Wu, L., Hase, F., Kivi, R., Wunch, D., Pollard, D. F., Shiomi, K., Deutscher, N. M., Velasco, V. A., Roehl, C. M., Wennberg, P. O., Warneke, T., and Landgraf, J.: Methane retrieved from TROPOMI: improvement of the data product and validation of the first 2 years of measurements, *Atmos. Meas. Tech.*, 14, 665–684, <https://doi.org/10.5194/amt-14-665-2021>, 2021.

- Lu, X., Jacob, D. J., Zhang, Y., Maasakkers, J. D., Sulprizio, M. P., Shen, L., Qu, Z., Scarpelli, T. R., Nesser, H., Yantosca, R. M., Sheng, J., Andrews, A., Parker, R. J., Boesch, H., Bloom, A. A., and Ma, S.: Global methane budget and trend, 2010–2017: complementarity of inverse analyses using in situ (GLOBALVIEWplus CH₄ ObsPack) and satellite (GOSAT) observations, *Atmos. Chem. Phys.*, 21, 4637–4657, <https://doi.org/10.5194/acp-21-4637-2021>, 2021.
- 710 Lu, X., Jacob, D. J., Wang, H., Maasakkers, J. D., Zhang, Y., Scarpelli, T. R., Shen, L., Qu, Z., Sulprizio, M. P., Nesser, H., Bloom, A. A., Ma, S., Worden, J. R., Fan, S., Parker, R. J., Boesch, H., Gautam, R., Gordon, D., Moran, M. D., Reuland, F., Villasana, C. A. O., and Andrews, A.: Methane emissions in the United States, Canada, and Mexico: evaluation of national methane emission inventories and 2010–2017 sectoral trends by inverse analysis of in situ (GLOBALVIEWplus CH₄ ObsPack) and satellite (GOSAT) atmospheric observations, *Atmos. Chem. Phys.*, 22, 395–418, <https://doi.org/10.5194/acp-22-395-2022>, 2022.
- Lu, Y.Y., Zhang, H.D., Zhou, Z., Ge, Z.L., Chen, C.J., Hou, Y.D. and Ye, M.L.: Current status and effective suggestions for efficient exploitation of coalbed methane in China: a review. *Energy & Fuels*, 35(11), 9102-9123, <https://doi.org/10.1021/acs.energyfuels.1c00460>, 2021.
- 720 Lyon, D.R., Zavala-Araiza, D., Alvarez, R.A., Harriss, R., Palacios, V., Lan, X., Talbot, R., Lavoie, T., Shepson, P., Yacovitch, T.I. and Herndon, S.C.: Constructing a spatially resolved methane emission inventory for the Barnett Shale region. *Environ. Sci. Technol.*, 49(13), 8147-8157, <https://doi.org/10.1021/es506359c>, 2015.
- Ma, S., Worden, J.R., Bloom, A.A., Zhang, Y., Poulter, B., Cusworth, D.H., Yin, Y., Pandey, S., Maasakkers, J.D., Lu, X. and Shen, L.: Satellite constraints on the latitudinal distribution and temperature sensitivity of wetland methane emissions. *AGU Advances*, 2(3), p.e2021AV000408, <https://doi.org/10.1029/2021AV000408>, 2021.
- 730 Maasakkers, J.D., Jacob, D.J., Sulprizio, M.P., Turner, A.J., Weitz, M., Wirth, T., Hight, C., DeFigueiredo, M., Desai, M., Schmeltz, R. and Hockstad, L.: Gridded national inventory of US methane emissions. *Environ. Sci. Technol.*, 50(23), 13123-13133, <https://doi.org/10.1021/acs.est.6b02878>, 2016.
- Maasakkers, J. D., Jacob, D. J., Sulprizio, M. P., Scarpelli, T. R., Nesser, H., Sheng, J.-X., Zhang, Y., Hersher, M., Bloom, A. A., Bowman, K. W., Worden, J. R., Janssens-Maenhout, G., and Parker, R. J.: Global distribution of methane emissions, emission trends, and OH concentrations and trends inferred from an inversion of GOSAT satellite data for 2010–2015, *Atmos. Chem. Phys.*, 19, 7859–7881, <https://doi.org/10.5194/acp-19-7859-2019>, 2019.
- 740 Maasakkers, J.D., Varon, D.J., Elfarsdóttir, A., McKeever, J., Jervis, D., Mahapatra, G., Pandey, S., Lorente, A., Borsdorff, T., Foorthuis, L.R. and Schuit, B.J.: Using satellites to uncover large methane emissions from landfills, *Earth ArXiv*, <https://doi.org/10.31223/X5N33G>, 2022.
- Miller, S. M., Michalak, A. M., and Levi, P. J.: Atmospheric inverse modeling with known physical bounds: an example from trace gas emissions, *Geosci. Model Dev.*, 7, 303–315, <https://doi.org/10.5194/gmd-7-303-2014>, 2014.

- Miller, S.M., Michalak, A.M., Detmers, R.G., Hasekamp, O.P., Bruhwiler, L.M. and Schwietzke, S.: China's coal mine methane regulations have not curbed growing emissions. *Nat. Commun.*, 10(1), 1-8, <https://doi.org/10.1038/s41467-018-07891-7>, 2019.
- 750 Naik, V., S. Szopa, B. Adhikary, P. Artaxo, T. Berntsen, W. D. Collins, S. Fuzzi, L. Gallardo, A. Kiendler Scharr, Z. Klimont, H. Liao, N. Unger, P. Zanis: Short-Lived Climate Forcers. In: *Climate Change 2021: The Physical Science Basis. Contribution of Working Group I to the Sixth Assessment Report of the Intergovernmental Panel on Climate Change* [Masson-Delmotte, V., P. Zhai, A. Pirani, S. L. Connors, C. Péan, S. Berger, N. Caud, Y. Chen, L. Goldfarb, M. I. Gomis, M. Huang, K. Leitzell, E. Lonnoy, J. B. R. Matthews, T. K. Maycock, T. Waterfield, O. Yelekçi, R. Yu and B. Zhou (eds.)]. Cambridge University Press. In Press, 2021.
- Palmer, P.I., Feng, L., Lunt, M.F., Parker, R.J., Bösch, H., Lan, X., Lorente, A. and Borsdorff, T.: The added value of satellite observations of methane for understanding the contemporary methane budget. *Philos. Trans. R. Soc. A*, 379(2210), p.20210106, <https://doi.org/10.1098/rsta.2021.0106>, 2021.
- 760 Pandey, S., Houweling, S., Krol, M., Aben, I., Chevallier, F., Dlugokencky, E. J., Gatti, L. V., Gloor, E., Miller, J. B., Detmers, R., Machida, T., and Röckmann, T.: Inverse modeling of GOSAT-retrieved ratios of total column CH₄ and CO₂ for 2009 and 2010, *Atmos. Chem. Phys.*, 16, 5043–5062, <https://doi.org/10.5194/acp-16-5043-2016>, 2016.
- Parker, R. J., Webb, A., Boesch, H., Somkuti, P., Barrio Guillo, R., Di Noia, A., Kalaitzi, N., Anand, J. S., Bergamaschi, P., Chevallier, F., Palmer, P. I., Feng, L., Deutscher, N. M., Feist, D. G., Griffith, D. W. T., Hase, F., Kivi, R., Morino, I., Notholt, J., Oh, Y.-S., Ohyama, H., Petri, C., Pollard, D. F., Roehl, C., Sha, M. K., Shiomi, K., Strong, K., Sussmann, R., Té, Y., Velasco, V. A., Warneke, T., Wennberg, P. O., and Wunch, D.: A decade of GOSAT Proxy satellite CH₄ observations, *Earth Syst. Sci. Data*, 12, 3383–3412, <https://doi.org/10.5194/essd-12-3383-2020>, 2020.
- 770 Peng, S., Piao, S., Bousquet, P., Ciais, P., Li, B., Lin, X., Tao, S., Wang, Z., Zhang, Y., and Zhou, F.: Inventory of anthropogenic methane emissions in mainland China from 1980 to 2010, *Atmos. Chem. Phys.*, 16, 14545–14562, <https://doi.org/10.5194/acp-16-14545-2016>, 2016.
- Prather, M.J., Holmes, C.D. and Hsu, J.: Reactive greenhouse gas scenarios: Systematic exploration of uncertainties and the role of atmospheric chemistry. *Geophys. Res. Lett.*, 39(9), <https://doi.org/10.1029/2012GL051440>, 2012.
- Qin, Y., Tong, F., Yang, G. and Mauzerall, D.L.: Challenges of using natural gas as a carbon mitigation option in China. *Energy Policy*, 117, 457-462, <https://doi.org/10.1016/j.enpol.2018.03.004>, 2018.
- 780 Qu, Z., Jacob, D. J., Shen, L., Lu, X., Zhang, Y., Scarpelli, T. R., Nesser, H., Sulprizio, M. P., Maasakkers, J. D., Bloom, A. A., Worden, J. R., Parker, R. J., and Delgado, A. L.: Global distribution of methane emissions: a comparative inverse analysis of observations from the TROPOMI and GOSAT satellite instruments, *Atmos. Chem. Phys.*, 21, 14159–14175, <https://doi.org/10.5194/acp-21-14159-2021>, 2021.
- Rutherford, J.S., Sherwin, E.D., Ravikumar, A.P., Heath, G.A., Englander, J., Cooley, D., Lyon, D., Omara, M., Langfitt, Q. and Brandt, A.R.: Closing the methane gap in US oil and natural gas

production emissions inventories. *Nat. Commun.*, 12(1), 1-12, <https://doi.org/10.1038/s41467-021-25017-4>, 2021.

790 Sadavarte, P., Pandey, S., Maasackers, J.D., Lorente, A., Borsdorff, T., Denier van der Gon, H., Houweling, S. and Aben, I.: Methane Emissions from Superemitting Coal Mines in Australia Quantified Using TROPOMI Satellite Observations. *Environ. Sci. Technol.*, 55(24), 16573-16580, <https://doi.org/10.1021/acs.est.1c03976>, 2021.

Sánchez-García, E., Gorroño, J., Irakulis-Loitxate, I., Varon, D. J., and Guanter, L.: Mapping methane plumes at very high spatial resolution with the WorldView-3 satellite, *Atmos. Meas. Tech.*, 15, 1657–1674, <https://doi.org/10.5194/amt-15-1657-2022>, 2022.

800 Saunio, M., Stavert, A. R., Poulter, B., Bousquet, P., Canadell, J. G., Jackson, R. B., Raymond, P. A., Dlugokencky, E. J., Houweling, S., Patra, P. K., Ciais, P., Arora, V. K., Bastviken, D., Bergamaschi, P., Blake, D. R., Brailsford, G., Bruhwiler, L., Carlson, K. M., Carrol, M., Castaldi, S., Chandra, N., Crevoisier, C., Crill, P. M., Covey, K., Curry, C. L., Etiope, G., Frankenberg, C., Gedney, N., Hegglin, M. I., Höglund-Isaksson, L., Hugelius, G., Ishizawa, M., Ito, A., Janssens-Maenhout, G., Jensen, K. M., Joos, F., Kleinen, T., Krummel, P. B., Langenfelds, R. L., Laruelle, G. G., Liu, L., Machida, T., Maksyutov, S., McDonald, K. C., McNorton, J., Miller, P. A., Melton, J. R., Morino, I., Müller, J., Murguia-Flores, F., Naik, V., Niwa, Y., Noce, S., O'Doherty, S., Parker, R. J., Peng, C., Peng, S., Peters, G. P., Prigent, C., Prinn, R., Ramonet, M., Regnier, P., Riley, W. J., Rosentreter, J. A., Segers, A., Simpson, I. J., Shi, H., Smith, S. J., Steele, L. P., Thornton, B. F., Tian, H., Tohjima, Y., Tubiello, F. N., Tsuruta, A., Viovy, N., Voulgarakis, A., Weber, T. S., van Weele, M., van der Werf, G. R., Weiss, R. F., Worthy, D., Wunch, D., Yin, Y., Yoshida, Y., Zhang, W., Zhang, Z., Zhao, Y., Zheng, B., Zhu, Q., Zhu, Q., and Zhuang, Q.: The Global Methane Budget 2000–2017, *Earth Syst. Sci. Data*, 12, 1561–1623, <https://doi.org/10.5194/essd-12-1561-2020>, 2020.

810 Scarpelli, T.R., Jacob, D.J., Villasana, C.A.O., Hernández, I.F.R., Moreno, P.R.C., Alfaro, E.A.C., García, M.Á.G. and Zavala-Araiza, D.: A gridded inventory of anthropogenic methane emissions from Mexico based on Mexico's national inventory of greenhouse gases and compounds. *Environ. Res. Lett.*, 15(10), p.105015, <https://orcid.org/0000-0001-5544-8732>, 2020a.

820 Scarpelli, T. R., Jacob, D. J., Maasackers, J. D., Sulprizio, M. P., Sheng, J.-X., Rose, K., Romeo, L., Worden, J. R., and Janssens-Maenhout, G.: A global gridded ($0.1^\circ \times 0.1^\circ$) inventory of methane emissions from oil, gas, and coal exploitation based on national reports to the United Nations Framework Convention on Climate Change, *Earth Syst. Sci. Data*, 12, 563–575, <https://doi.org/10.5194/essd-12-563-2020>, 2020b.

Scarpelli, T. R., Jacob, D. J., Grossman, S., Lu, X., Qu, Z., Sulprizio, M. P., Zhang, Y., Reuland, F., Gordon, D., and Worden, J. R.: Updated Global Fuel Exploitation Inventory (GFEI) for methane emissions from the oil, gas, and coal sectors: evaluation with inversions of atmospheric methane observations, *Atmos. Chem. Phys.*, 22, 3235–3249, <https://doi.org/10.5194/acp-22-3235-2022>, 2022.

Schuldt, K. N, et al: Multi-laboratory compilation of atmospheric methane data for the period 1983-2020; obspack_ch4_1_GLOBALVIEWplus_v4.0_2021-10-14; NOAA Earth System Research Laboratory, Global Monitoring Laboratory, <http://doi.org/10.25925/20211001>, 2021.

- 830 Shen, L., Zavala-Araiza, D., Gautam, R., Omara, M., Scarpelli, T., Sheng, J., Sulprizio, M.P., Zhuang, J., Zhang, Y., Qu, Z. and Lu, X.: Unravelling a large methane emission discrepancy in Mexico using satellite observations. *Remote Sens. Environ.*, 260, p.112461, <https://doi.org/10.1016/j.rse.2021.112461>, 2021.
- Shen, L., Gautam, R., Omara, M., Zavala-Araiza, D., Maasakkers, J., Scarpelli, T., Lorente, A., Lyon, D., Sheng, J., Varon, D., Nesser, H., Qu, Z., Lu, X., Sulprizio, M., Hamburg, S., and Jacob, D.: Satellite quantification of oil and natural gas methane emissions in the US and Canada including contributions from individual basins, *Atmos. Chem. Phys. Discuss.*, <https://doi.org/10.5194/acp-2022-155>, in review, 2022.
- 840 Sheng, J., Song, S., Zhang, Y., Prinn, R.G. and Janssens-Maenhout, G.: Bottom-up estimates of coal mine methane emissions in China: a gridded inventory, emission factors, and trends. *Environ. Sci. Technol. Lett.*, 6(8), 473-478, <https://doi.org/10.1021/acs.estlett.9b00294>, 2019.
- Turner, A. J. and Jacob, D. J.: Balancing aggregation and smoothing errors in inverse models, *Atmos. Chem. Phys.*, 15, 7039–7048, <https://doi.org/10.5194/acp-15-7039-2015>, 2015.
- Turner, A. J., Jacob, D. J., Wecht, K. J., Maasakkers, J. D., Lundgren, E., Andrews, A. E., Biraud, S. C., Boesch, H., Bowman, K. W., Deutscher, N. M., Dubey, M. K., Griffith, D. W. T., Hase, F., Kuze, A., Notholt, J., Ohyama, H., Parker, R., Payne, V. H., Sussmann, R., Sweeney, C., Velasco, V. A., Warneke, T., Wennberg, P. O., and Wunch, D.: Estimating global and North American methane emissions with high spatial resolution using GOSAT satellite data, *Atmos. Chem. Phys.*, 15, 7049–7069, <https://doi.org/10.5194/acp-15-7049-2015>, 2015.
- 850 Wang, X., Liu, C., Chen, S., Chen, L., Li, K. and Liu, N.: Impact of coal sector’s de-capacity policy on coal price. *Applied Energy*, 265, p.114802, <https://doi.org/10.1016/j.apenergy.2020.114802>, 2020.
- Wecht, K. J., Jacob, D. J., Sulprizio, M. P., Santoni, G. W., Wofsy, S. C., Parker, R., Bösch, H., and Worden, J.: Spatially resolving methane emissions in California: constraints from the CalNex aircraft campaign and from present (GOSAT, TES) and future (TROPOMI, geostationary) satellite observations, *Atmos. Chem. Phys.*, 14, 8173–8184, <https://doi.org/10.5194/acp-14-8173-2014>, 2014.
- 860 Wolf, J., Asrar, G.R. and West, T.O.: Revised methane emissions factors and spatially distributed annual carbon fluxes for global livestock. *Carbon balance manag.*, 12(1), 1-24, <https://doi.org/10.1186/s13021-017-0084-y>, 2017.
- Worden, J., Cusworth, D., Qu, Z., Yin, Y., Zhang, Y., Bloom, A. A., Ma, S., Byrne, B., Scarpelli, T. R., Maasakkers, J., Crisp, D., Duren, R., and Jacob, D.: The 2019 Methane Budget And Uncertainties At 1 Degree Resolution And Each Country Through Bayesian Integration Of GOSAT Total Column Methane Data And A Priori Inventory Estimates, *Atmos. Chem. Phys. Discuss.*, <https://doi.org/10.5194/acp-2021-955>, in review, 2021.
- van der Werf, G. R., Randerson, J. T., Giglio, L., van Leeuwen, T. T., Chen, Y., Rogers, B. M., Mu, M., van Marle, M. J. E., Morton, D. C., Collatz, G. J., Yokelson, R. J., and Kasibhatla, P. S.: Global fire emissions estimates during 1997–2016, *Earth Syst. Sci. Data*, 9, 697–720, <https://doi.org/10.5194/essd-9-697-2017>, 2017.

- 870 van Peet, J., Houweling, S., Marshall, J., Nunez Ramirez, T. and Segers, A.: Inverse modelling of global methane emissions using TROPOMI. In EGU General Assembly Conference Abstracts (EGU21-14510), 2021.
- Varon, D. J., Jacob, D. J., Sulprizio, M., Estrada, L., Downs, W. B., Shen, L., Hancock, S. E., Nesser, H., Qu, Z., Penn, E., Chen, Z., Lu, X., Lorente, A., Tewari, A., and Randles, C. A.: Integrated Methane Inversion (IMI 1.0): A user-friendly, cloud-based facility for inferring high-resolution methane emissions from TROPOMI satellite observations, *Geosci. Model Dev. Discuss.*, <https://doi.org/10.5194/gmd-2022-45>, in review, 2022.
- Xu, A., Wu, Y.H., Chen, Z., Wu, G., Wu, Q., Ling, F., Huang, W.E. and Hu, H.Y.: Towards the new era of wastewater treatment of China: development history, current status, and future directions. *Water Cycle*, 1, 80-87, <https://doi.org/10.1016/j.watcyc.2020.06.004>, 2020.
- 880 Yuan, B., et al., Airborne flux measurements of methane and volatile organic compounds over the Haynesville and Marcellus shale gas production regions, *J. Geophys. Res. Atmos.*, 120, 6271–6289, doi:10.1002/2015JD023242, 2015.
- Zavala-Araiza, D., Lyon, D.R., Alvarez, R.A., Davis, K.J., Harriss, R., Herndon, S.C., Karion, A., Kort, E.A., Lamb, B.K., Lan, X. and Marchese, A.J.: Reconciling divergent estimates of oil and gas methane emissions. *Proc. Natl. Acad. Sci. U.S.A.*, 112(51), 15597-15602, <https://doi.org/10.1073/pnas.1522126112>, 2015.
- Zhang, B., Tian, H., Ren, W., Tao, B., Lu, C., Yang, J., Banger, K. and Pan, S.: Methane emissions from global rice fields: Magnitude, spatiotemporal patterns, and environmental controls. *Global Biogeochem. Cycles*, 30(9), 1246-1263, <https://doi.org/10.1002/2016GB005381>, 2016.
- 890 Zhang, Y., Gautam, R., Pandey, S., Omara, M., Maasackers, J.D., Sadavarte, P., Lyon, D., Nesser, H., Sulprizio, M.P., Varon, D.J. and Zhang, R.: Quantifying methane emissions from the largest oil-producing basin in the United States from space. *Sci. Adv.*, 6(17), p.eaaz5120, <https://doi.org/10.1126/sciadv.aaz5120>, 2020.
- Zhang, Y., Jacob, D. J., Lu, X., Maasackers, J. D., Scarpelli, T. R., Sheng, J.-X., Shen, L., Qu, Z., Sulprizio, M. P., Chang, J., Bloom, A. A., Ma, S., Worden, J., Parker, R. J., and Boesch, H.: Attribution of the accelerating increase in atmospheric methane during 2010–2018 by inverse analysis of GOSAT observations, *Atmos. Chem. Phys.*, 21, 3643–3666, <https://doi.org/10.5194/acp-21-3643-2021>, 2021.
- 900 Zhu, T., Bian, W., Zhang, S., Di, P. and Nie, B.: An improved approach to estimate methane emissions from coal mining in China. *Environ. Sci. Technol.*, 51(21), 12072-12080, <https://doi.org/10.1021/acs.est.7b01857>, 2017.

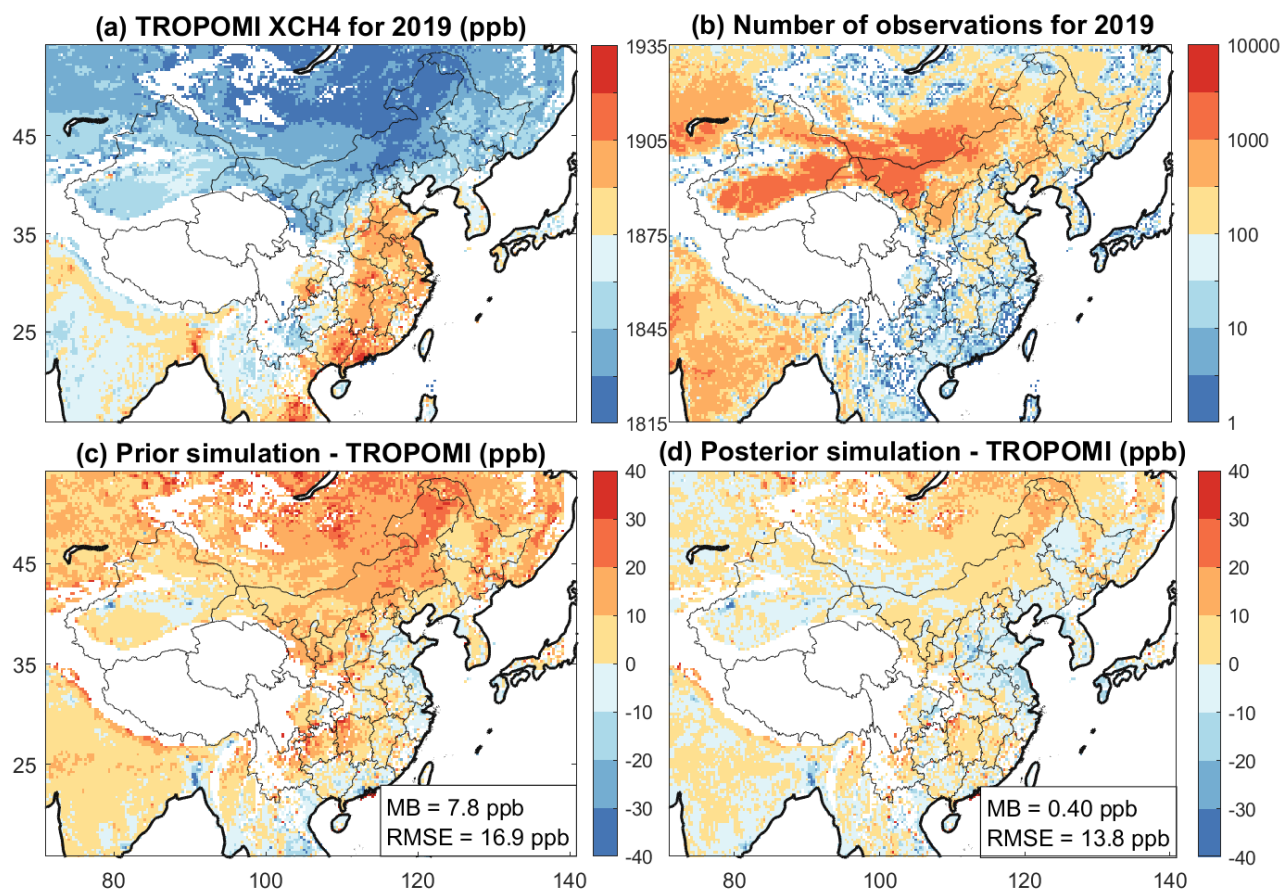
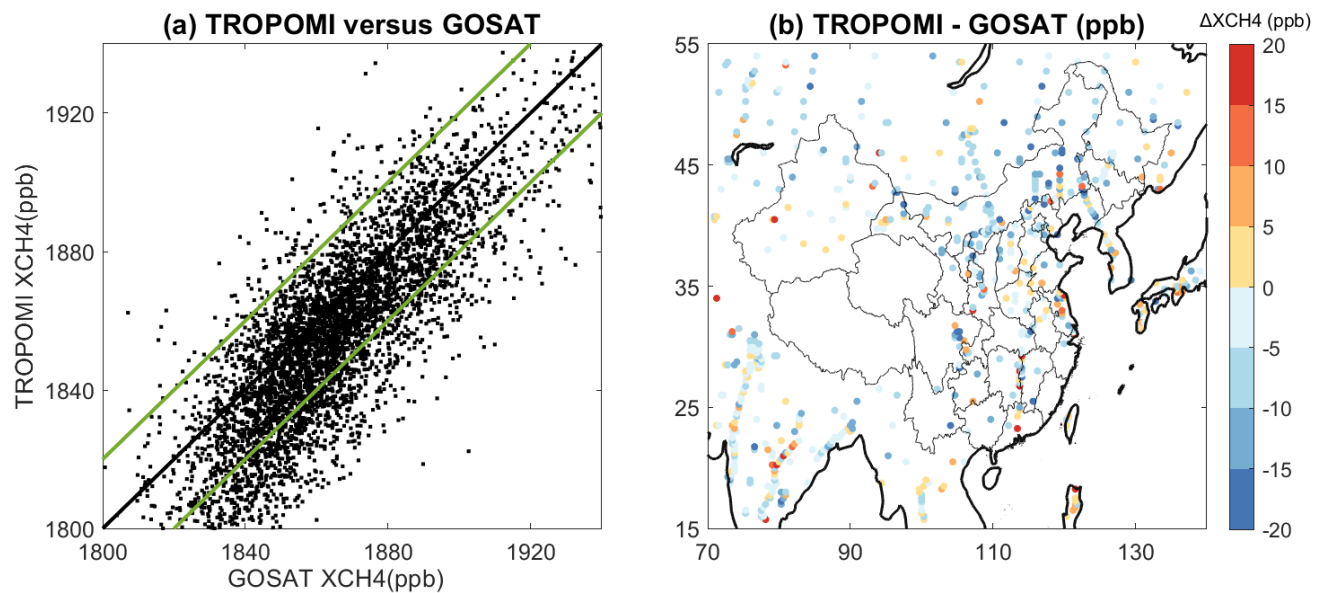


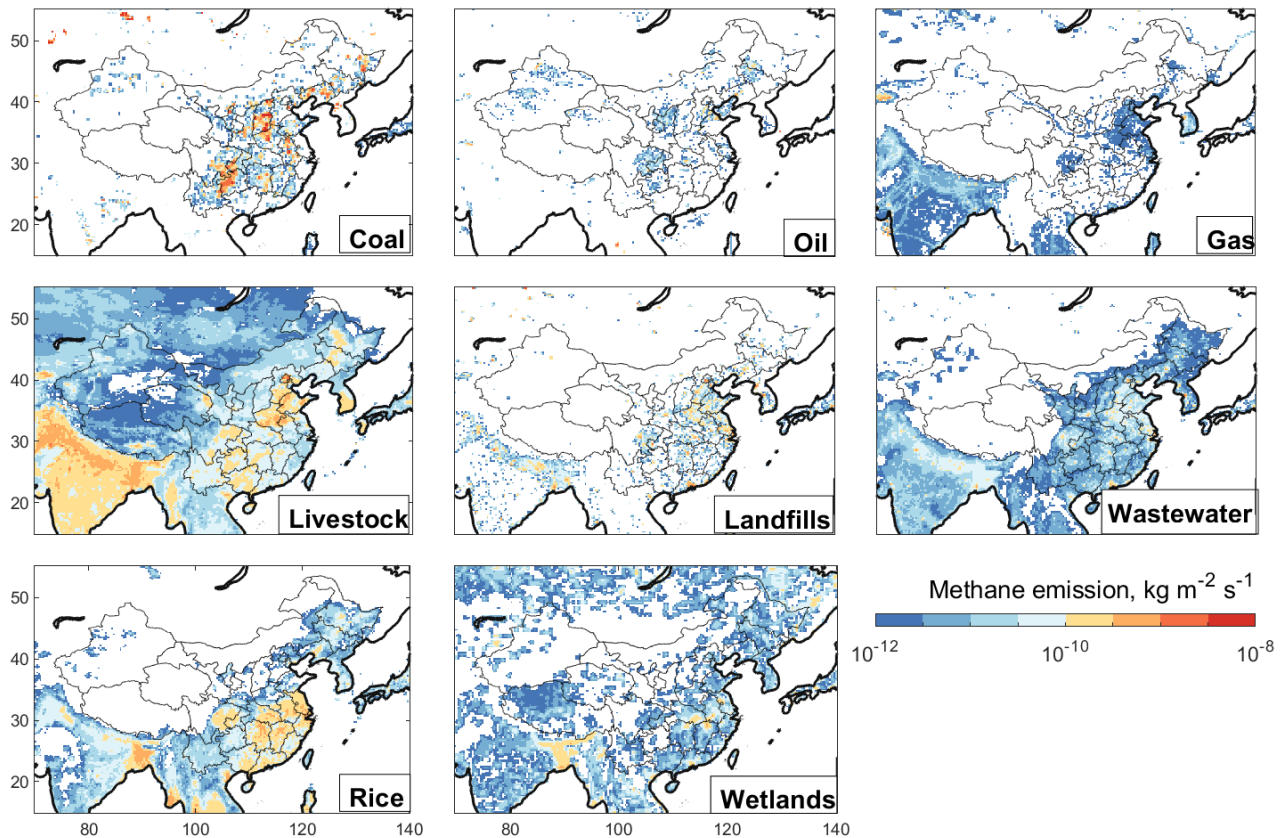
Figure 1. TROPOMI observations of column-averaged dry methane mixing ratios (XCH_4) over East Asia and comparison to GEOS-Chem simulations. (a) Mean observations for 2019 mapped on the GEOS-Chem $0.25^\circ \times 0.3125^\circ$ grid. (b) Number of observations on that grid. (c) Mean differences between the GEOS-Chem simulation with prior emissions and observations. The spatiotemporal mean bias (MB) and root-mean-square error (RMSE) over the study domain are shown inset. (d) Same as (c) but for the GEOS-Chem simulation with posterior emissions. Thin black lines are Chinese provincial boundaries.



930

Figure 2. Comparison between 2019 TROPOMI and GOSAT observations of XCH₄ over East Asia. (a) Scatter plot of daily observations on the GEOS-Chem 0.25° × 0.3125° grid. Green lines indicate absolute TROPOMI-GOSAT differences of 20 ppb and we exclude the outlying TROPOMI observations. (b) Spatial pattern of annual mean differences ΔXCH_4 between TROPOMI and GOSAT observations after outlying TROPOMI data have been excluded. The mean difference is -3.6 ± 9.1 ppb. TROPOMI version 2.02 observations are from *Lorente et al.* (2021) and GOSAT version 9.0 observations are from *Parker et al.* (2020).

940



950

Figure 3. Prior estimates of methane emissions used for the inversion. Coal, oil, and gas emissions are from the GFEIv2 gridded version of the national inventories from individual countries reported to the UNFCCC (*Scarpelli et al., 2022*). Other anthropogenic emissions for China are from its UNFCCC report with spatial allocation from EDGAR v4.3.2, while for other countries they are from EDGAR v4.3.2. Wetland emissions are 2019 monthly means of the nine-member high-performance subset of the WetCHARTs inventory ensemble (*Ma et al., 2021*) and are shown here as the annual means for 2019. White areas have emissions lower than 1×10^{-12} kg m⁻² s⁻¹. Total emissions for China are listed in Table 1.

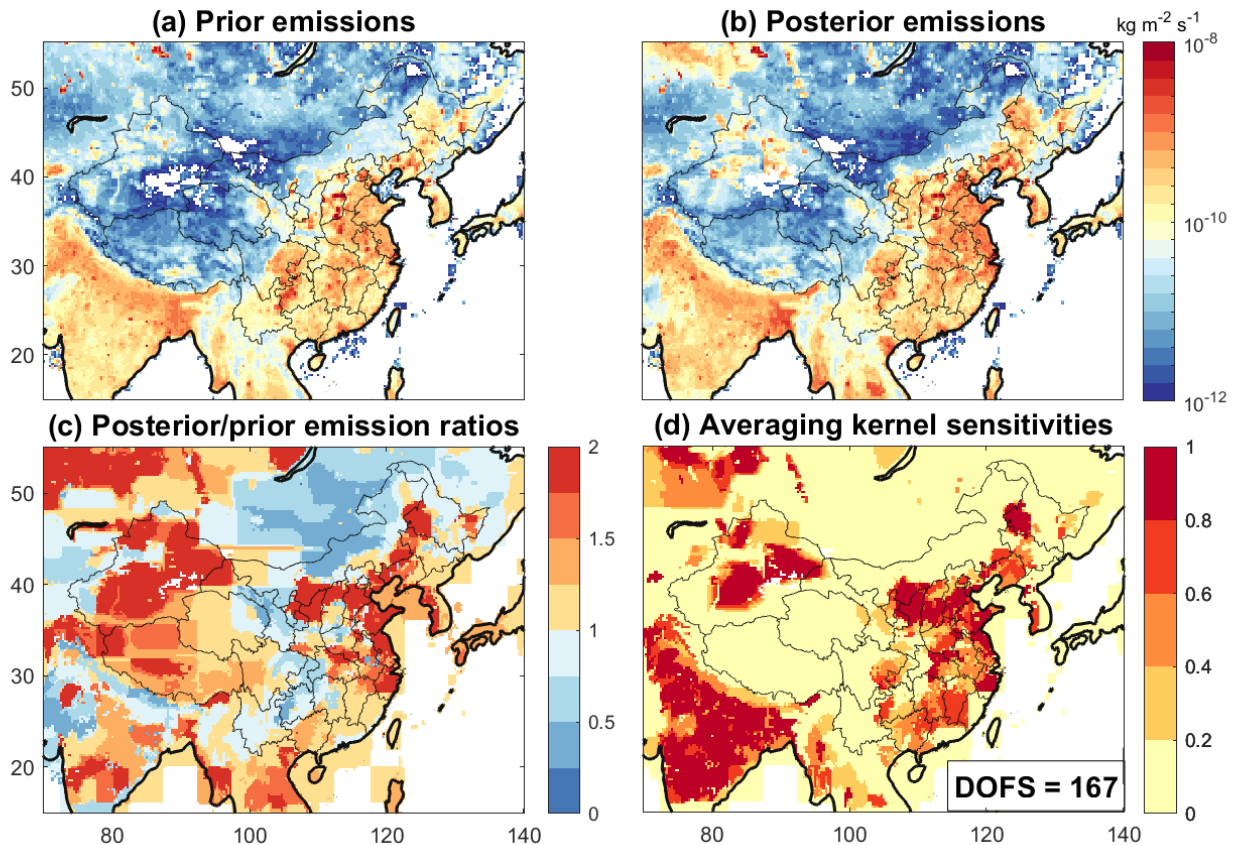


Figure 4. Optimization of methane emissions over East Asia in 2019 from inversion of TROPOMI observations. Results are from the base inversion and are shown on the $0.25^\circ \times 0.3125^\circ$ grid. (a) Prior estimates of methane emissions, summing the contributions from the sectors in Fig. 3 plus additional minor sectors as given in Table 1. (b) Posterior methane emissions from the TROPOMI inversion. (c) Posterior/prior emission ratios. (d) Averaging kernel sensitivities. The averaging kernel sensitivities are the diagonal elements of the averaging kernel matrix and display the ability of the observations to quantify emissions independently from the prior estimates (1 = fully, 0 = not at all). The degrees of freedom for signal (DOFS, defined as the trace of the averaging kernel matrix) is given inset.

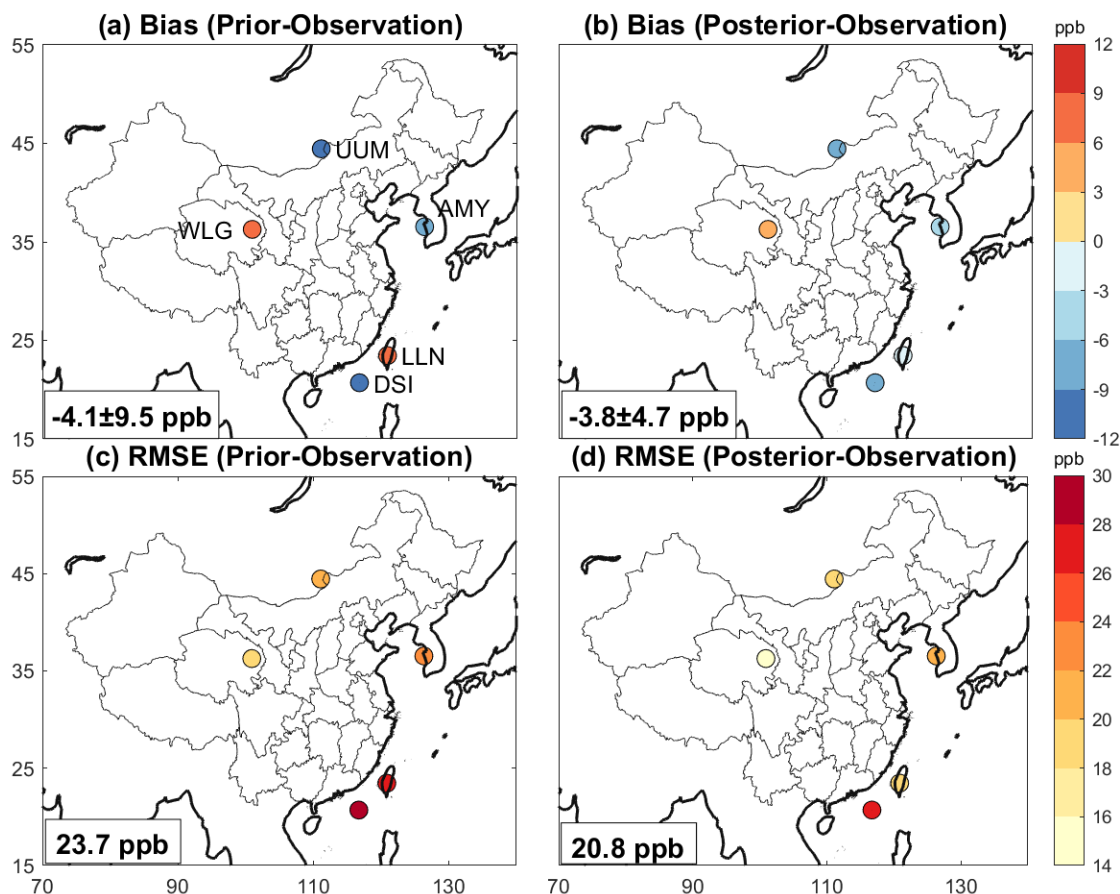


Figure 5. Comparison of GEOS-Chem simulations of atmospheric methane concentrations to *in situ* observations from five surface sites in 2019 compiled in the NOAA GLOBALVIEWplus CH₄ ObsPack v4.0 database. The five sites are described in detail in Table S2. The annual mean GEOS-Chem model biases and root-mean-square errors (RMSEs) for individual near-weekly observations at each site are shown. The insets give spatial mean biases \pm standard deviations for the ensemble of sites and corresponding RMSEs.

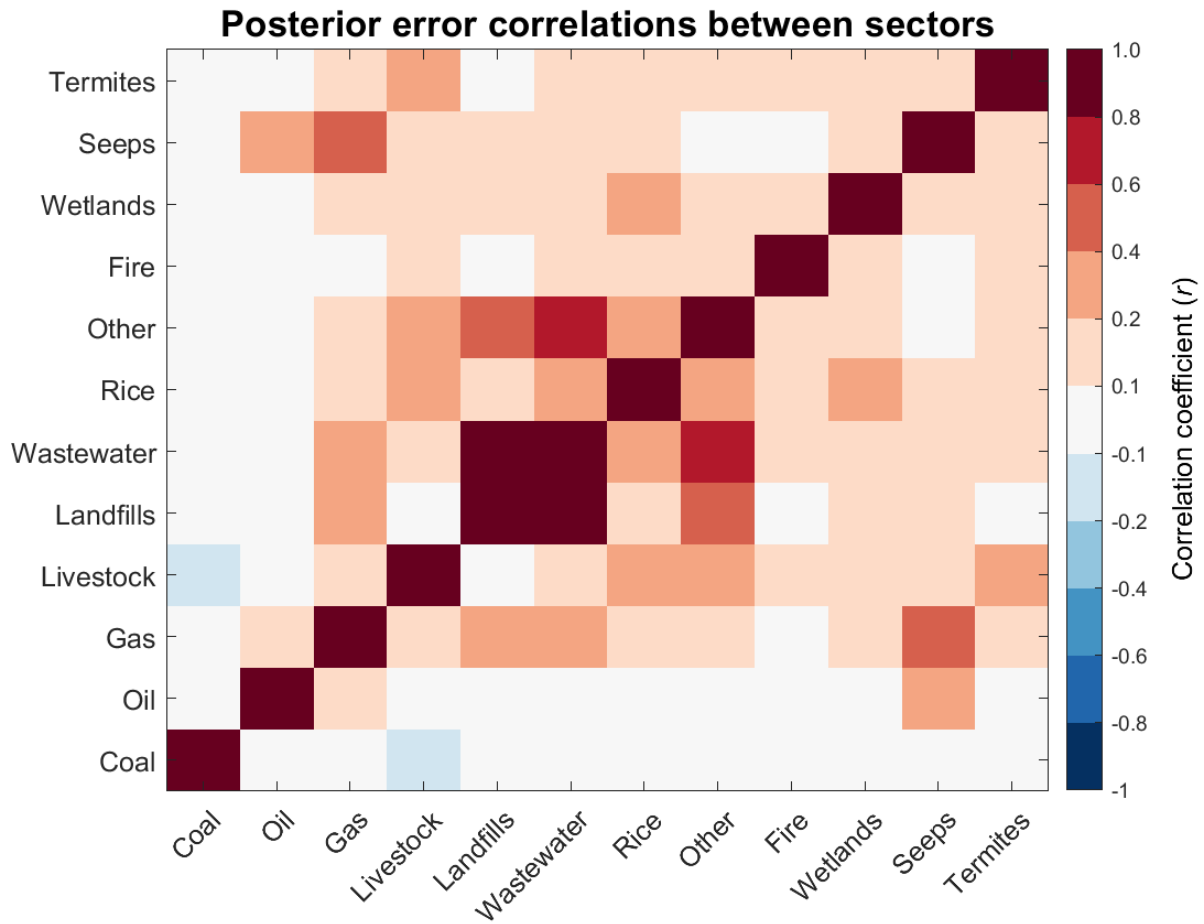


Figure 6. Error correlation coefficients (r) between posterior estimates of methane emissions from different source sectors in China. Error correlations measure the ability of the inversion to separate emissions between sectors (± 1 : not at all; 0: fully). ‘Other’ is a combination of minor anthropogenic emissions including industry, stationary combustion, mobile combustion, aircraft, composting, and field burning of agricultural residues.

1000

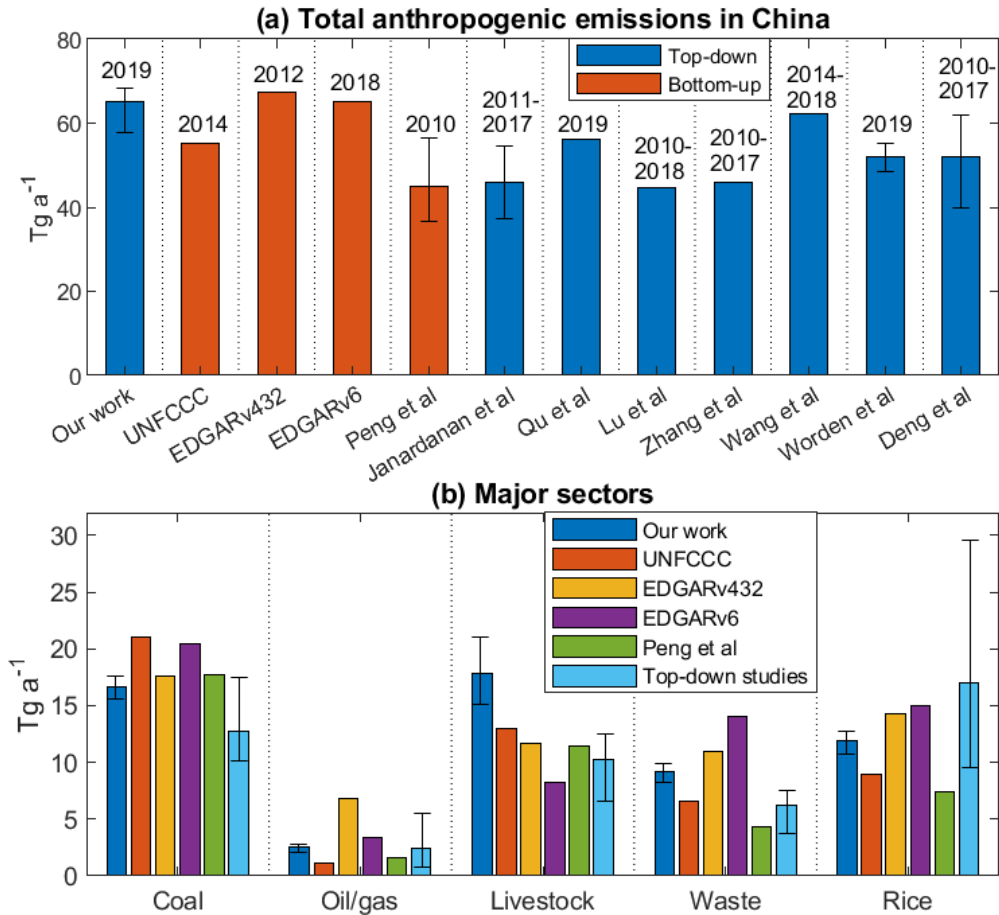


Figure 7. Anthropogenic methane emissions in China. The top panel compares the national total emissions reported by different bottom-up and top-down studies. Vertical bars for our work indicate the uncertainty range, obtained by combining results from the inversion ensemble and the posterior error covariance $\hat{\mathbf{S}}$ (Fig. S1). *Peng et al* (2016), *Janardanan et al* (2020), *Worden et al* (2022), and *Deng et al* (2022) also reported uncertainty estimates. The bottom panel shows the contributions from different sectors inferred in our work and compared to inventories including the UNFCCC, EDGAR, and *Peng et al* (2016), and to the means and ranges from recent top-down studies compiled in Table S3.

1010

1020

Table 1. Methane emissions in China in 2019.

	Prior estimate (Tg a⁻¹)^a	Posterior estimate (Tg a⁻¹)^b	Sensitivity to observations^c
Total emission	56.8	70.0 (61.6-79.9)	0.91
Anthropogenic	53.6	65.0 (57.7-68.4)	0.91
Coal mining	19.5	16.6 (15.6-17.6)	0.91
Oil	0.93	2.3 (1.8-2.5)	0.76
Gas ^d	0.18	0.29 (0.23-0.32)	0.30
Livestock ^e	13.0	17.8 (15.1-21.0)	0.75
Waste ^f	6.6	9.3 (8.2-9.9)	0.71
Rice paddies	8.9	11.9 (10.7-12.7)	0.86
Other ^g	4.6	6.7 (5.8-7.1)	0.81
Natural	3.2	5.0 (3.9-11.6)	0.61
Open fires ^h	0.16	0.24 (0.18-0.26)	0.30
Wetlands	2.3	3.4 (2.8-7.5)	0.61
Seeps	0.06	0.11 (0.10-0.18)	0.43
Termites	0.72	1.2 (0.8-3.7)	0.32

^aPrior estimates of anthropogenic emissions are from the Chinese government report to the UNFCCC for 2014 (*UNFCCC*, 2020). Wetland emissions are the mean of the high-performance subset of the WetCHARTs v1.3.1 inventory ensemble for 2019 (*Ma et al*, 2021). Open-fire emissions are from GFED4s (*van der Werf et al.*, 2017). Termite emissions are from *Fung et al* (1991), and geological seepage emissions are from *Etiopie et al* (2019) with scaling from *Hmiel et al.* (2020). See Sect. 2.2 for details.

1030 ^bResults from the base inversion, with uncertainty range in parentheses encompassing the best estimates from the inversion ensemble and the 2-sigma error from the posterior error covariance matrix $\hat{\mathbf{S}}$ of the base inversion (Fig. S1). See Sect. 2.6 for details.

^cSensitivity of posterior emissions to the TROPOMI observations, ranging from 0 (no information from observations, emissions determined by prior estimate) to 1 (full information from observations, no sensitivity to prior estimate). The sensitivities are defined by the diagonal terms of the reduced averaging kernel matrix for the inversion. See Sect. 2.5 for details.

^dContributions from production, transmission, and distribution sub-sectors are 0.03, 0.025, and 0.125 Tg a⁻¹ in the prior estimate, and are 0.07, 0.06, and 0.16 Tg a⁻¹ in the posterior estimate.

^eLivestock sector includes emissions from enteric fermentation and manure management.

1040 ^fWaste sector includes emissions from landfills and wastewater treatment, and are combined in the inversion because of their spatial overlap. Prior estimates are 3.84 Tg a⁻¹ for landfills and 2.72 Tg a⁻¹ for wastewater treatment.

^gIncluding industry, stationary combustion, mobile combustion, aircraft, composting, and field burning of agricultural residues.

^hExcluding field burning of agricultural residues.